

# High-energy radiation and pair production by Coulomb processes in particle-in-cell simulations

Cite as: Phys. Plasmas **26**, 103109 (2019); <https://doi.org/10.1063/1.5118339>

Submitted: 03 July 2019 • Accepted: 03 October 2019 • Published Online: 23 October 2019

 B. Martinez,  M. Lobet, R. Duclous, et al.



View Online



Export Citation



CrossMark

## ARTICLES YOU MAY BE INTERESTED IN

### Relativistic plasma physics in supercritical fields

Physics of Plasmas **27**, 050601 (2020); <https://doi.org/10.1063/1.5144449>

### Gamma photons and electron-positron pairs from ultra-intense laser-matter interaction: A comparative study of proposed configurations

Matter and Radiation at Extremes **4**, 064403 (2019); <https://doi.org/10.1063/1.5098978>

### Are we ready to transfer optical light to gamma-rays?

Physics of Plasmas **26**, 053103 (2019); <https://doi.org/10.1063/1.5090992>

Physics of Plasmas

Papers from 62nd Annual Meeting of the  
APS Division of Plasma Physics

Read now!



# High-energy radiation and pair production by Coulomb processes in particle-in-cell simulations

Cite as: Phys. Plasmas **26**, 103109 (2019); doi: [10.1063/1.5118339](https://doi.org/10.1063/1.5118339)

Submitted: 3 July 2019 · Accepted: 3 October 2019 ·

Published Online: 23 October 2019



View Online



Export Citation



CrossMark

B. Martinez,<sup>1,2,a)</sup> M. Lobet,<sup>3</sup> R. Duclous,<sup>1</sup> E. d'Humières,<sup>2</sup> and L. Gremillet<sup>1,b)</sup>

## AFFILIATIONS

<sup>1</sup>CEA, DAM, DIF, F-91297 Arpajon, France

<sup>2</sup>CELIA, UMR 5107, Université de Bordeaux-CNRS-CEA, 33405 Talence, France

<sup>3</sup>Maison de la Simulation, CEA, CNRS, Université Paris-Sud, UVSQ, Université Paris-Saclay, F-91191 Gif-sur-Yvette, France

<sup>a)</sup>Electronic mail: [bertrand.martinez8@gmail.com](mailto:bertrand.martinez8@gmail.com)

<sup>b)</sup>Electronic mail: [laurent.gremillet@cea.fr](mailto:laurent.gremillet@cea.fr)

## ABSTRACT

We present a Monte Carlo implementation of Bremsstrahlung, Bethe-Heitler, and Coulomb Trident processes into the particle-in-cell (PIC) simulation framework. In order to address photon emission and electron-positron pair productions in a wide range of physical conditions, we derive the Bremsstrahlung and Bethe-Heitler cross sections taking account of screening effects in arbitrary ionized plasmas. Our calculations are based on a simple model for the atomic Coulomb potential that describes shielding due to both bound electrons, free electrons, and ions. We then detail a pairwise particle interaction algorithm suited to weighted PIC plasma simulations, for which we perform several validation tests. Finally, we carry out a parametric study of photon and pair production during high-energy electron transport through micrometric solid foils. Compared to the zero-dimensional model of Myatt *et al.* [Phys. Rev. E **76**, 066409 (2009)], our integrated one-dimensional simulations pinpoint the importance of the electron energy losses resulting from the plasma expansion.

Published under license by AIP Publishing. <https://doi.org/10.1063/1.5118339>

## I. INTRODUCTION

Continuous progress in laser technology now makes available high-energy (0.1–1 kJ), short duration (0.1–1 ps) pulses, yielding focused intensities in excess of  $10^{20}$  Wcm<sup>-2</sup>. Such laser parameters may give rise to a regime of laser-matter interaction where collective plasma processes are coupled with strong radiation and electron-positron ( $e^-e^+$ ) pair production.<sup>1</sup> Most of the theoretical studies conducted in the past years have addressed the impact of the synchrotron photon emission and Breit-Wheeler pair production that result from the interaction of the laser field with, respectively, high-energy electrons and photons, and are expected to prevail at ultrahigh laser intensities ( $I_L \gtrsim 10^{22}$  Wcm<sup>-2</sup>).<sup>2–10</sup> While such extreme conditions should be achieved by the upcoming multipetawatt laser systems (e.g., CILEX-Apollon,<sup>11</sup> CoReLS,<sup>12</sup> CAEP-PW,<sup>13</sup> ELI<sup>14</sup>), current experiments operate at significantly lower intensities and are mostly prone to triggering Bremsstrahlung photon emission and Bethe-Heitler (or Trident) pair production which, instead of the laser field, are mediated by the Coulomb field of atomic nuclei.<sup>15–17</sup>

The incoherent Bremsstrahlung spectra originating from the interaction of laser-driven fast electrons with matter are a well-known

feature of high-intensity laser-solid experiments, which can serve for fast-electron characterization or radiography purposes.<sup>18–29</sup> In the same context, the generation of  $e^-e^+$  pairs directly follows from the Bremsstrahlung  $\gamma$ -ray photons interacting with heavy ions.<sup>30–37</sup> Record positron densities of  $\sim 10^{16}$  cm<sup>-3</sup> have been reported using millimeter-sized high-Z targets in which the Bethe-Heitler process mainly accounts for pair production. These thick targets are either directly irradiated by intense picosecond lasers<sup>32</sup> or penetrated by wakefield-driven electron beams originating from a laser-irradiated gas jet.<sup>38–40</sup> From measurements performed at various laser facilities, the positron yield has been found to scale approximately quadratically with the laser energy, owing to increasingly energetic electrons when rising the laser intensity and to their enhanced recirculation through the target.<sup>34</sup> While quasinneutral pair beams have been reported to be generated using wakefield-driven relativistic electrons,<sup>39</sup> the laser-solid experiments carried out so far have led to somewhat reduced  $e^-e^+$  density ratios ( $n_+/n_- \sim 0.5$ ), as recently measured at the Texas Petawatt Laser Facility.<sup>41</sup>

The particle-in-cell (PIC) technique<sup>42</sup> is widely used to simulate the kinetic and collective phenomena at play in intense laser-plasma interactions. In anticipation of the future multipetawatt laser

experiments, much effort has been lately made worldwide to enrich PIC codes with numerical models describing the synchrotron photon emission and the Breit-Wheeler pair production.<sup>8,43–47</sup> Since these processes are mediated by electromagnetic fields, they mainly take place within the laser-irradiated region and thus do not require increasing the typical space-time scales of the laser-plasma simulation. By contrast, the Coulomb-field-mediated processes of radiation (Bremsstrahlung) and pair production (Bethe-Heitler and Trident) arise during the relaxation of the laser-driven relativistic electrons through the dense target, and therefore over time ( $\sim 1 - 10$  ps) and (approximately millimeter) scales usually much larger than those characterizing the laser interaction. As this puts strong computational constraints on integrated PIC simulations, the radiation and pair production physics in current laser experiments are typically modeled using dedicated Monte Carlo (MC) codes with input fast-electron sources estimated from theoretical arguments, PIC simulations, or experimental data.<sup>32,38,48–51</sup>

Although a full-scale, self-consistent modeling of the Coulomb-field-mediated radiation and pair production in intense laser-solid interactions is still outside the reach of multidimensional PIC codes, it remains worthwhile to study these effects over the restricted space-time scales currently accessible to simulations. This has motivated a number of groups to implement Bremsstrahlung<sup>52–56</sup> and Bethe-Heitler<sup>57,58</sup> packages into PIC codes. All of these works employ a Monte Carlo (MC) approach based on analytical<sup>15</sup> or tabulated<sup>59</sup> cross sections, which are expected to be most valid for isolated neutral atoms. Since intense laser-solid interactions may lead to a variety of ionization states, and hence atomic screening effects, it is useful to provide more general cross sections in view of their implementation into particle-in-cell Monte Carlo (PIC-MC) laser-plasma simulation codes. This is the first objective of the present article. The second one is to present a Monte Carlo pairwise interaction scheme, which is adapted to macroparticles with arbitrary numerical weights. Finally, we apply our numerical model to the investigation of pair production during fast-electron transport within a self-consistent simulation framework.

This paper is organized as follows. In Sec. II, by combining the theoretical formulas reviewed in Refs. 15 and 60 with a mixed Thomas-Fermi-Debye screened atomic potential,<sup>61–63</sup> we derive a set of modified Bremsstrahlung and Bethe-Heitler cross sections valid for partially ionized dense plasmas. These expressions, supplemented with the Coulomb Trident cross section<sup>17</sup> for direct pair production, form the basis of a Monte Carlo package included in the PIC-MC CALDER code, describing Coulomb-mediated radiation and pair production processes. Our numerical implementation, detailed in Sec. III A, relies on a macroparticle-pairing algorithm that handles arbitrary weighted macroparticles, originally developed for modeling elastic Coulomb collisions.<sup>64,65</sup> In Sec. III B, we demonstrate the capability of CALDER to accurately model the total (collisional-radiative) electronic stopping power of a solid target in a broad range of electron energies, while in Sec. IV, we study the positron generation accompanying the relaxation of fast electrons inside a solid copper foil of variable thickness. Finally, we summarize our results in Sec. V.

## II. BREMSSTRAHLUNG AND PAIR PRODUCTION CROSS SECTIONS IN PARTIALLY IONIZED PLASMAS

In this section, we obtain analytic cross sections for the electron Bremsstrahlung and Bethe-Heitler processes, taking account of the

Thomas-Fermi- and Debye-type screening effects in a unified fashion depending on the plasma parameters.

### A. Simple atomic potential model

The Coulomb interaction between a high-energy electron and an ion's nucleus is modified by the screening due to bound electrons, free electrons, and plasma ions, as a function of the ionization state of the medium. For neutral atoms of atomic number  $Z$ , the Coulomb potential around the nuclear charge can be assumed to be of the Yukawa type

$$V_{\text{TF}}(r) = \frac{q}{r} \exp(-r/L_{\text{TF}}), \quad (1)$$

$$L_{\text{TF}} = 4\pi\epsilon_0 \frac{\hbar^2}{m_e e^2} Z^{-1/3}, \quad (2)$$

where  $q = Ze/4\pi\epsilon_0$ , and  $L_{\text{TF}}$  is the Thomas-Fermi length accounting for shielding by bound electrons. We have introduced  $\epsilon_0$  the permittivity of free space,  $m_e$  the electron mass,  $e$  the elementary charge, and  $\hbar = h/2\pi$  the Planck constant. More precise multiexponential fits of the Thomas-Fermi potential could be used,<sup>66</sup> but we will limit ourselves to the above simple approximation. While Eq. (2) applies, in principle, to an isolated neutral atom (where charge neutrality is fulfilled at infinity), we assume that it also holds in a cold neutral medium (where charge neutrality is fulfilled at the ion-sphere radius).<sup>67</sup>

In a highly ionized plasma, the Coulomb potential can be modeled in a similar form

$$V_{\text{D}}(r) = \frac{q}{r} \exp(-r/L_{\text{D}}), \quad (3)$$

$$L_{\text{D}} = \sqrt{\frac{\epsilon_0 k_{\text{B}} T}{e^2 n_i Z^* (Z^* + 1)}}, \quad (4)$$

where  $L_{\text{D}}$  is the Debye length that describes the screening by free electrons and plasma ions,  $Z^*$  is the ionization degree,  $k_{\text{B}}$  is the Boltzmann constant, and  $n_i$  is the ion density. We have supposed a globally neutral plasma ( $n_e = Z^* n_i$ ) and equal electron and ion temperatures ( $T_e = T_i = T$ ). To address coupled plasma regimes, we impose a lower bound on  $L_{\text{D}}$ , equal to the interatomic distance<sup>68</sup>  $r_i = (3/4\pi n_i)^{1/3}$ . In practice, the ionization degree  $Z^*$  is evaluated using a numerical fit to the Thomas-Fermi model for a finite-radius atom.<sup>69</sup>

In the general case of a partially ionized plasma, following Refs. 61 and 63, we assume for simplicity that the Coulomb potential can be described as a weighted sum of the above Thomas-Fermi and Debye screened potentials

$$V_{\text{TFD}}(r) = \frac{q_{\text{TF}}}{r} \exp(-r/L_{\text{TF}}) + \frac{q_{\text{D}}}{r} \exp(-r/L_{\text{D}}), \quad (5)$$

with  $q_{\text{TF}}/q = 1 - Z^*/Z$  and  $q_{\text{D}}/q = (Z^*/Z)$ . In a cold neutral medium ( $Z^* \rightarrow 0$ ), we have  $V_{\text{TFD}} \rightarrow V_{\text{TF}}$ , whereas, in a fully ionized plasma,  $V_{\text{TFD}} \rightarrow V_{\text{D}}$ , as expected. Also,  $V_{\text{TFD}}(r) \rightarrow Ze/4\pi\epsilon_0 r$  when  $r \rightarrow 0$  as it should. More accurate screening models could be used<sup>70</sup> but at the expense of analytical simplicity.

### B. Bremsstrahlung cross sections

Let us consider an electron of total energy  $E_1/m_e c^2 = \gamma_1$  and normalized momentum  $p_1 = \sqrt{\gamma_1^2 - 1}$ , both measured in the ion rest

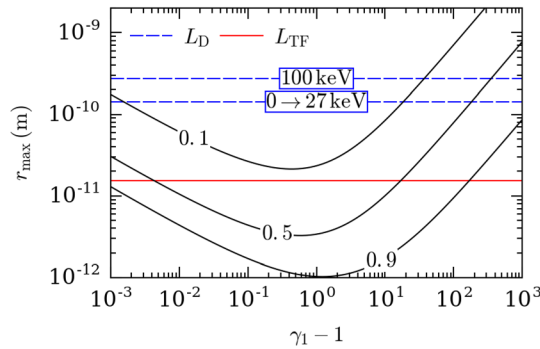


**FIG. 1.** Maximum impact parameter  $r_{\max}$  (solid black curves) vs normalized electron kinetic energy for relative photon energies  $k/(\gamma_1 - 1) \in (0.1, 0.5, 0.9)$ . The Debye screening length ( $L_D$ ) is plotted for a solid-density Cu plasma of temperature  $T \in (0, 27)$  keV and  $T = 100$  keV (dashed blue lines). In the former case,  $L_D$  is bounded by the interatomic distance. The Thomas-Fermi screening length ( $L_{TF}$ ) is plotted as a red line.

frame. After emitting a photon of normalized energy  $k = \hbar\omega/m_e c^2$  in the screened atomic field, the normalized electron energy and momentum become  $\gamma_2 = \gamma_1 - k$  and  $p_2 = \sqrt{\gamma_2^2 - 1}$ , respectively. Let us introduce  $r_C = \hbar/m_e c$  as the Compton radius. For given electron and ion parameters, the importance of screening effects on Bremsstrahlung can be assessed by comparing the maximum impact parameter,  $r_{\max} = r_C/(p_1 - p_2 - k)$ , with the Thomas-Fermi and Debye screening lengths.<sup>15</sup> If  $r_{\max}$  is much smaller than  $L_{TF}$  or  $L_D$ , then the corresponding screening process is expected to be negligible. Figure 1 plots  $r_{\max}$  as a function of the normalized electron kinetic energy,  $\gamma_1 - 1$ , for various relative photon energies  $k/(\gamma_1 - 1) \in (0.1, 0.5, 0.9)$ . Overlaid are plots of  $L_{TF}$  and  $L_D$  in a solid-density copper plasma of variable temperature ( $T \leq 27$  keV and  $T = 100$  keV). At the solid density, the Debye length defined by Eq. (4) exceeds the interatomic distance ( $r_i = 1.4 \times 10^{-10}$  m) only at temperatures of  $> 27$  keV. From this graph, both Thomas-Fermi and Debye shielding effects should be more pronounced at very high, and to a lesser degree, low electron energies; besides, at a fixed electron energy, they should be enhanced with a decreasing photon energy.

In the following, the photon-energy-differential Bremsstrahlung cross sections are derived based on the atomic potential (5). As per our knowledge, there is no general analytic theory for electron energies varying from the keV to the GeV ranges, we draw upon the results of Ref. 15, and make use of three distinct formulae, respectively, valid for (i) nonrelativistic ( $1 < \gamma_1 \lesssim 2$ ), (ii) moderately relativistic ( $2 \lesssim \gamma_1 \lesssim 100$ ), and (iii) ultrarelativistic ( $\gamma_1 \gtrsim 100$ ) electron energies.

### 1. Nonrelativistic electrons

Introducing  $\tilde{V}_{TFD}(\mathbf{u})$  the Fourier transform of  $V_{TFD}(\mathbf{r})$ , normalized by the factor  $e/(\alpha_f m_e c^2)$

$$\tilde{V}_{TFD}(\mathbf{u}) = \frac{1}{(2\pi)^3} \int \frac{e V_{TFD}(\mathbf{r})}{\alpha_f m_e c^2} \exp(i \mathbf{u} \cdot \mathbf{r}) d^3 \left( \frac{\mathbf{r}}{r_C} \right), \quad (6)$$

the nonrelativistic ( $1 < \gamma_1 \leq 2$ ) electron Bremsstrahlung cross section, differential in the photon energy, writes in the Born approximation<sup>71</sup>

$$\frac{d\sigma_{Br,nr,TFD}}{dk} = \frac{64\pi^4 r_e^2 \alpha_f}{3k p_1^2} \int_{\delta p_-}^{\delta p_+} |\tilde{V}_{TFD}(u)|^2 u^3 du. \quad (7)$$

Here,  $\alpha_f = e^2/(4\pi\epsilon_0 \hbar c)$  denotes the fine structure constant,  $r_e = e^2/(4\pi\epsilon_0 m_e c^2)$  is the classical electron radius, and  $\delta p_+ = 2p_1 - k$  and  $\delta p_- = k$  are, respectively, the maximum and minimum momentum transfers to the nucleus in the collision.

After substituting Eqs. (5) and (6) into Eq. (7), one obtains the nonrelativistic Bremsstrahlung cross section (see Appendix A)

$$\frac{d\sigma_{Br,nr,TFD}}{dk} = \frac{16r_e^2 Z^2 \alpha_f}{3k p_1^2} [g(\delta p_+, \delta p_-, \eta_{TF}, \bar{L}_{TF}) + g(\delta p_+, \delta p_-, \eta_D, \bar{L}_D) + \Gamma_c], \quad (8)$$

where we have introduced the function  $g$

$$g(\delta p_+, \delta p_-, \eta, L) = \frac{\eta^2}{2} \left[ \ln \left( \frac{\delta p_+^2 \bar{L}^2 + 1}{\delta p_-^2 \bar{L}^2 + 1} \right) + \frac{1}{\delta p_+^2 \bar{L}^2 + 1} - \frac{1}{\delta p_-^2 \bar{L}^2 + 1} \right], \quad (9)$$

and the coupling term  $\Gamma_c$

$$\Gamma_c = \frac{\eta_{TF} \eta_D}{(\bar{L}_D^2 - \bar{L}_{TF}^2)} \left[ \bar{L}_{TF}^2 \ln \left( \frac{\delta p_-^2 \bar{L}_D^2 + 1}{\delta p_+^2 \bar{L}_D^2 + 1} \right) + \bar{L}_D^2 \ln \left( \frac{\delta p_+^2 \bar{L}_{TF}^2 + 1}{\delta p_-^2 \bar{L}_{TF}^2 + 1} \right) \right] \quad (10)$$

with  $\eta_{TF} = q_{TF}/q = 1 - Z^*/Z$ ,  $\eta_D = q_D/q = Z^*/Z$ , and  $\bar{L}$  denotes lengths, normalized by the Compton radius:  $\bar{L} = L/r_C$ .

As is well known,<sup>72</sup> the accuracy of the Born approximation can be improved in the nonrelativistic regime by multiplying Eq. (8) by the Elwert correction factor<sup>72,73</sup>

$$f_E = \frac{\beta_1}{\beta_2} \frac{1 - \exp(-2\pi Z \alpha_f / \beta_1)}{1 - \exp(-2\pi Z \alpha_f / \beta_2)}. \quad (11)$$

Figure 2 displays the Elwert-corrected cross section,  $k d\sigma_{Br,nr,TFD}/dk$  (red curve), as a function of the normalized photon energy  $k/(\gamma_1 - 1)$

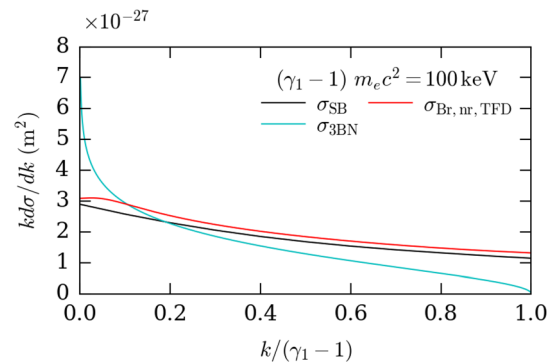


**FIG. 2.** Nonrelativistic Bremsstrahlung cross section  $k d\sigma/dk$  vs normalized photon energy  $k/(\gamma_1 - 1)$  for a 100 keV energy electron interacting with the neutral Cu atoms. Comparison between the Elwert-corrected formula ( $k d\sigma_{Br,nr,TFD}/dk$ , red curve), Seltzer and Berger's data<sup>59</sup> ( $k d\sigma_{SB}/dk$ , black curve), and the nonscreened formula 3BN of Ref. 15 ( $k d\sigma_{3BN}/dk$ , cyan curve).

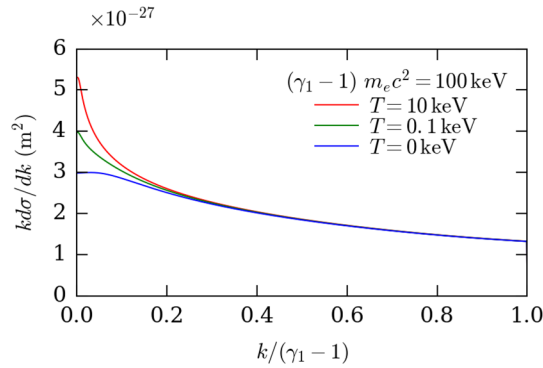


**FIG. 3.** Nonrelativistic Bremsstrahlung cross section  $k d\sigma_{\text{Br,nr,TFD}}/dk$  vs normalized photon energy  $k/(\gamma_1 - 1)$  for a 100 keV electron in a solid-density Cu plasma of temperature ranging from  $T = 0$  to 10 keV.

for a 100 keV energy electron interacting with neutral Cu atoms (where the Debye shielding vanishes). On the same graph are plotted the reference tabulated data of Seltzer and Berger,<sup>59</sup>  $\sigma_{\text{SB}}$  (black curve), and the nonscreened cross section for a point Coulomb potential (formula 3BN in Ref. 15),  $\sigma_{\text{3BN}}$  (cyan curve). The difference between  $k d\sigma_{\text{SB}}/dk$  and  $k d\sigma_{\text{3BN}}/dk$  is most pronounced at high and low photon energies owing to, respectively, Coulomb and screening effects. By contrast, we observe that the Elwert-corrected screened cross section satisfactorily reproduces Seltzer and Berger's data over the full photon energy range. For completeness, we have measured the relative error, averaged over photon energies  $0 < k/(\gamma_1 - 1) \leq 1$  and in the 1–500 keV kinetic energy range, between  $k d\sigma_{\text{Br,nr,TFD}}/dk$  and  $k d\sigma_{\text{SB}}/dk$ . This error is maximum (78%) for 1 keV electrons, decreases down to 17% for 50 keV electrons, and rises again up to 53% for 500 keV electrons. This difference is expected to increase in higher- $Z$  materials for which the Born approximation ( $2\pi Z/137\beta_1 \ll 1$ ) becomes less valid.

Figure 3 quantifies the effect of the Debye shielding on  $k d\sigma_{\text{Br,nr,TFD}}/dk$  as a function of the target temperature (and the corresponding ionization). The electron kinetic energy is still set to 100 keV, while the temperature of the solid-density Cu target is varied in the range  $0 \leq T \leq 10$  keV. The observed behavior is consistent with the prediction of Fig. 1 that screening effects weaken at high photon energies: While, as expected, all curves tend to coincide at high photon energies, the cross section  $k d\sigma/dk$  at low photon energies [ $k/(\gamma_1 - 1) \lesssim 0.1$ ] is seen to rise (by up to  $\sim 60\%$  for  $k \rightarrow 0$ ) with the target temperature. This variation originates from the increasing effective screening length, which evolves from  $L_{\text{TF}}$  at low temperatures to  $L_{\text{D}}$  at high temperatures. As  $L_{\text{D}}$  is about one order of magnitude larger than  $L_{\text{TF}}$  (see Fig. 1), a strongly ionized plasma allows for electron-nucleus interactions at larger impact parameters, thus increasing the cross section. Since screening corrections mainly concern the low-energy side of the spectrum, their impact on the total radiative stopping power remains weak: The latter increases by a mere 7% increase when the temperature rises from 0 to 10 keV.

## 2. Moderately relativistic electrons

For moderately relativistic electrons ( $2 \leq \gamma_1 \leq 100$ ), the photon-energy-differential Bremsstrahlung cross section is given by the following expression, valid for arbitrary screening:<sup>15,74</sup>

$$\frac{d\sigma_{\text{Br,r,TFD}}}{dk} = \frac{4Z^2 r_e^2 \alpha_f}{k} \left\{ \left[ 1 + \left( \frac{\gamma_1 - k}{\gamma_1} \right)^2 \right] [I_1(\delta) + 1] - \frac{2}{3} \frac{\gamma_1 - k}{\gamma_1} \left[ I_2(\delta) + \frac{5}{6} \right] \right\}, \quad (12)$$

where the functions  $I_1$  and  $I_2$  account for screening effects

$$I_1(\delta) = \int_{\delta}^1 \frac{du}{u^3} (u - \delta)^2 [1 - F_e(u)]^2, \quad (13)$$

$$I_2(\delta) = \int_{\delta}^1 \frac{du}{u^4} [u^3 - 6\delta^2 u \ln(u/\delta) + 3\delta^2 u - 4\delta^3] \times [1 - F_e(u)]^2. \quad (14)$$

The argument  $\delta = k/2\gamma_1(\gamma_1 - k)$  approximately measures the minimum momentum transfer to the atom in the limit  $\gamma_1, \gamma_2 \gg 1$ . The above functions involve the atomic form factor (see Appendix B)

$$1 - F_e(u) = \frac{2\pi^2}{Z} u^2 \tilde{V}(u). \quad (15)$$

For a simple single-exponential atomic potential,  $V(r) = (q/r) \exp(-r/L)$ , the integrals  $I_1$  and  $I_2$  can be exactly calculated (see Appendix B):

$$I_1 = \bar{L}\delta(\arctan(\delta\bar{L}) - \arctan\bar{L}) - \frac{\bar{L}^2(1-\delta)^2}{2(1+\bar{L}^2)} + \frac{1}{2} \ln \left( \frac{1+\bar{L}^2}{1+\bar{L}^2\delta^2} \right), \quad (16)$$

$$2I_2 = 4\bar{L}^3\delta^3[\arctan\bar{L}\delta - \arctan\bar{L}] + (1+3\bar{L}^2\delta^2) \ln \left( \frac{1+\bar{L}^2}{1+\bar{L}^2\delta^2} \right) + \frac{6\bar{L}^4\delta^2}{1+\bar{L}^2} \ln \delta + \frac{\bar{L}^2(\delta-1)(\delta+1-4\bar{L}^2\delta^2)}{1+\bar{L}^2}. \quad (17)$$

For the more general atomic potential  $V_{\text{TFD}}(r)$ , in contrast to  $I_1, I_2$  cannot be expressed in terms of elementary functions. However, drawing upon Ref. 75, an approximate analytical expression can be derived by matching the asymptotic expressions of Eq. (12) obtained in the limit  $\delta \rightarrow 0$  using the double-exponential potential  $V_{\text{TFD}}(r)$  and the single-exponential potential (hereafter referred to as the “reduced potential”),  $V_{\text{R}}(r)$ . To this goal, we make use of the asymptotic expression

$$I = \lim_{\delta \rightarrow 0} I_1 = \lim_{\delta \rightarrow 0} I_2 = \int_0^1 u^3 \left( \frac{1 - F_e(u)}{u^2} \right)^2 du. \quad (18)$$

This integral can be analytically evaluated for  $V_{\text{TFD}}$ , as detailed in Appendix C. Let  $I_{\text{TFD}}$  denote its solution:

$$I_{\text{TFD}} = \frac{q_{\text{TF}}^2}{2q^2} \frac{(1+\bar{L}_{\text{TF}}^2) \ln(1+\bar{L}_{\text{TF}}^2) - \bar{L}_{\text{TF}}^2}{1+\bar{L}_{\text{TF}}^2} + \frac{q_{\text{D}}^2}{2q^2} \frac{(1+\bar{L}_{\text{D}}^2) \ln(1+\bar{L}_{\text{D}}^2) - \bar{L}_{\text{D}}^2}{1+\bar{L}_{\text{D}}^2} + \frac{q_{\text{TF}}q_{\text{D}}}{q^2} \frac{\bar{L}_{\text{D}}^2 \ln(1+\bar{L}_{\text{TF}}^2) - \bar{L}_{\text{TF}}^2 \ln(1+\bar{L}_{\text{D}}^2)}{\bar{L}_{\text{D}}^2 - \bar{L}_{\text{TF}}^2}. \quad (19)$$



For the reduced potential  $V_R(r) = (q/r) \exp(-r/L_R)$ , where  $L_R$  is the sought-for reduced screening length, the solution to the above integral is

$$I_R = \frac{q_R^2}{2q^2} \frac{(1 + \bar{L}_R^2) \ln(1 + \bar{L}_R^2) - \bar{L}_R^2}{1 + \bar{L}_R^2}. \quad (20)$$

The asymptotic equality  $\lim_{\delta \rightarrow 0} d\sigma_{Br,r,TFD}/dk = \lim_{\delta \rightarrow 0} d\sigma_{Br,r,R}/dk$  implies  $I_{TFD} = I_R$ , which defines the equation solved by  $L_R$ . Setting  $a = I_{TFD}$ ,  $q_R = q$  and  $x = \bar{L}_R^2$ , this equation can be recast as

$$2a(x+1) = (x+1) \ln(x+1) - x. \quad (21)$$

The solution involves the Lambert  $W$ -function

$$\bar{L}_R \equiv \sqrt{x} = \left\{ \exp[W(-e^{-1-2a}) + 1 + 2a] - 1 \right\}^{1/2}. \quad (22)$$

As the coefficient  $a$  is positive,  $W$  varies over the interval  $[-1/e, 0]$ , so that  $\bar{L}_R$  is well defined. Combining Eqs. (12), (20), and (22) gives a closed form analytical expression for the cross section  $d\sigma_{Br,r,R}/dk$ .

In Fig. 4, we compare the Bremsstrahlung cross sections computed using the reduced analytical formula ( $kd\sigma_{Br,r,R}/dk$ , red curve) with Seltzer and Berger's reference data<sup>59</sup> ( $kd\sigma_{SB}/dk$ , black curve). The case of a 5 MeV electron energy and the neutral ( $Z^* = 0$ ) Cu atoms is considered. Note that in this limiting case of neutral atoms, the reduced potential ( $kd\sigma_{Br,r,R}/dk$ ) and the one numerically computed from the Thomas-Fermi-Debye potential ( $kd\sigma_{Br,r,TFD}/dk$ ) exactly coincide. Importantly, good agreement is found with Ref. 59, except near  $k/(\gamma_1 - 1) = 1$ , where a factor of  $\sim 2$  discrepancy is observed. Comparison with the unscreened relativistic cross section ( $kd\sigma_{3BN}/dk$ , cyan curve) confirms that shielding by bound electrons is mostly influential at low photon energies. Overall, the relative error, averaged over  $0 < k/(\gamma_1 - 1) < 1$ , between  $\sigma_{Br,r,R}/dk$  and  $d\sigma_{SB}/dk$  is found to steadily drop from  $\sim 49\%$  for 1 MeV electrons to  $\sim 26\%$  for 50 MeV electrons.

Figure 5 shows the thermal dependence of the Bremsstrahlung cross section in a solid-density Cu plasma. The incident electron energy is again set to 5 MeV. For temperature values  $0 \leq T \leq 10$  keV,

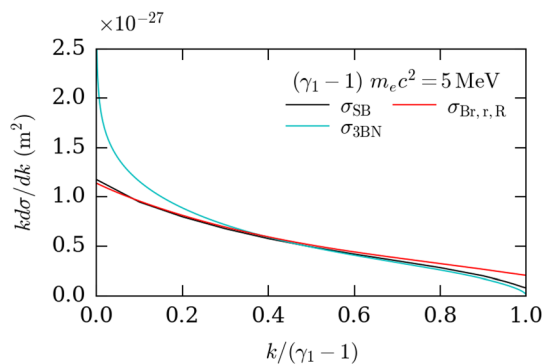


**FIG. 4.** Relativistic Bremsstrahlung cross section ( $kd\sigma/dk$ ) vs normalized photon energy for a 5 MeV electron interacting with the neutral Cu atoms. Comparison between the reduced analytical formula ( $kd\sigma_{Br,r,R}/dk$ , red curve), Seltzer and Berger's data<sup>59</sup> ( $\sigma_{SB}$ , black curve), and the unscreened formula 3BN<sup>15</sup> ( $\sigma_{3BN}$ , cyan curve).

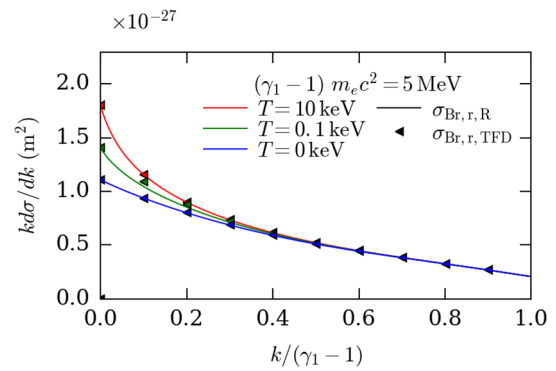


**FIG. 5.** Relativistic Bremsstrahlung cross section ( $kd\sigma/dk$ ) vs normalized photon energy for a 5 MeV electron in a solid-density Cu plasma of temperature ranging from  $T = 0$  to 10 keV. Comparison of the numerically computed cross section using the Thomas-Fermi-Debye potential ( $kd\sigma_{Br,r,TFD}/dk$ , symbols) with the reduced analytical formula ( $kd\sigma_{Br,r,R}/dk$ , solid lines).

one can see that the analytical cross section from the reduced potential (solid lines,  $kd\sigma_{Br,r,R}/dk$ ) closely reproduces that numerically computed with the Thomas-Fermi-Debye potential (symbols,  $kd\sigma_{Br,r,TFD}/dk$ ) over the full range of photon energies. As in the nonrelativistic regime (Fig. 3), Debye screening proves to be mainly significant at low relative photon energies, causing a  $\sim 60\%$  increase in the cross section when  $k \rightarrow 0$ . Still, this only translates into a quite modest 12% enhancement of the total radiated stopping power. Slightly larger enhancements are predicted with higher-energy electrons.

### 3. Ultrarelativistic electrons

For ultrarelativistic electron energies ( $\gamma_1 > 100$ ), the accuracy of the Born-approximation formula (12) can be improved by adding the Coulomb correction term  $-f_C(Z)$  as follows:<sup>15</sup>

$$\frac{d\sigma_{Br,ur,TFD}}{dk} = \frac{4Z^2 r_e^2 \alpha_f}{k} \left\{ \left[ 1 + \left( \frac{\gamma_1 - k}{\gamma_1} \right)^2 \right] [I_1(\delta) + 1 - f_C(Z)] - \frac{2}{3} \frac{\gamma_1 - k}{\gamma_1} \left[ I_2(\delta) + \frac{5}{6} - f_C(Z) \right] \right\}. \quad (23)$$

Introducing the Riemann function  $\zeta$ , the Coulomb correction term is defined as<sup>15</sup>

$$f_C(Z) = \frac{\alpha_f^2 Z^2}{1 + \alpha_f^2 Z^2} \sum_{n=0}^{\infty} \left( -\alpha_f^2 Z^2 \right)^n [\zeta(2n+1) - 1]. \quad (24)$$

In practice, keeping the first four terms has been found sufficient for an accurate computation of  $f_C$  even at high  $Z$  values.

Figure 6 shows that, for a 100 MeV energy electron in neutral copper, the Bremsstrahlung cross section based on the reduced potential ( $kd\sigma_{Br,ur,R}/dk$ , red curve) agrees well with Berger and Seltzer's data<sup>59</sup> ( $kd\sigma_{SB}/dk$ , black curve). Again, in the present case of neutral atoms, the reduced formula exactly coincides with that evaluated using the full Thomas-Fermi-Debye potential (not shown). By contrast, the unscreened ultrarelativistic formula from Ref. 15 ( $kd\sigma_{3BN}/dk$ , cyan curve) appears to overestimate the cross section by a factor of  $> 1.5$  at

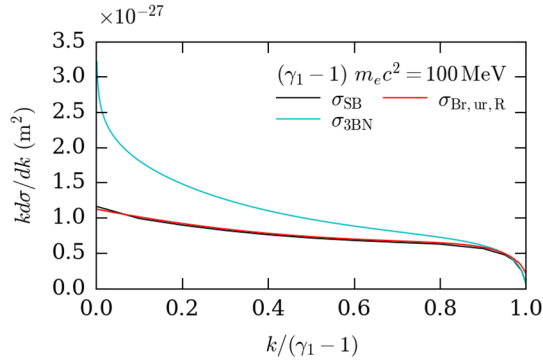


**FIG. 6.** Coulomb-corrected ultrarelativistic Bremsstrahlung cross section ( $kd\sigma/dk$ ) vs normalized photon energy for a 100 MeV electron interacting with the neutral Cu atoms. Comparison between the reduced analytical formula ( $kd\sigma_{Br,ur,R}/dk$ , red curve), Seltzer and Berger's data<sup>59</sup> ( $\sigma_{SB}$ , black curve), and the nonscreened formula 3BN<sup>15</sup> ( $\sigma_{3BN}$ , cyan curve).

photon energies  $k/(\gamma_1 - 1) \lesssim 0.2$ . More generally, the relative error, averaged over  $0 < k/(\gamma_1 - 1) < 1$ , between  $d\sigma_{Br,ur,R}/dk$  and  $d\sigma_{SB}/dk$  is measured to decrease from  $\sim 22\%$  for 60 MeV electrons to  $\sim 5\%$  for electron energies in the 0.5–10 GeV range.

Still for a 100 MeV energy electron, the thermal variations of the Bremsstrahlung cross section in solid Cu are displayed in Fig. 7 in the 0–10 keV temperature range. As in the moderately relativistic regime, the analytical formula based on the reduced potential closely matches the numerically evaluated cross section for all photon energies. In contrast to Fig. 5, though, where Debye screening only affects the emission of relatively low-energy photons [ $k/(\gamma_1 - 1) \lesssim 0.2$ ], it now significantly modifies the cross section up to photon energies  $k/(\gamma_1 - 1) \lesssim 0.7$ . This increased sensitivity of the photon spectrum to Debye shielding has a stronger impact on the radiative stopping power, which, in the present case, rises by  $\sim 37\%$  as the plasma temperature is increased from 0 to 10 keV.

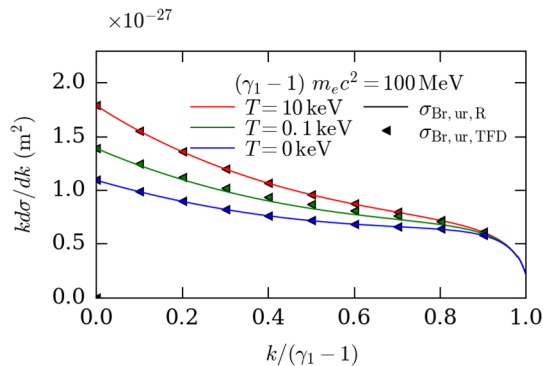


**FIG. 7.** Coulomb-corrected, ultrarelativistic Bremsstrahlung cross section ( $kd\sigma/dk$ ) vs normalized photon energy for a 100 MeV electron in a solid-density Cu plasma of temperature varying from 0 to 10 keV. Comparison of the numerically computed cross section using the Thomas-Fermi-Debye potential ( $kd\sigma_{Br,ur,TFD}/dk$ , symbols) with the reduced analytical formula ( $kd\sigma_{Br,ur,R}/dk$ , solid lines).

## C. Pair production cross sections

### 1. Bethe-Heitler process

The cross section of the Bethe-Heitler pair production by a photon of normalized energy  $k \gg 1$ , differential in the normalized positron energy  $\gamma_+$ , is given in the ion-rest frame by formula 3D-1003 of Ref. 60,

$$\frac{d\sigma_{BH,TFD}}{d\gamma_+} = \frac{4Z^2 r_e^2 \alpha_f}{k^3} \left\{ (\gamma_+^2 + \gamma_-^2) [I_1(\delta) + 1] + \frac{2}{3} \gamma_+ \gamma_- \left[ I_2(\delta) + \frac{5}{6} \right] \right\}, \quad (25)$$

where  $\delta = k/(2\gamma_+ \gamma_-)$ . This formula further assumes large electron and positron energies ( $\gamma_+, \gamma_- \gg 1$ ) and negligible nucleus recoil. We note that it bears much resemblance to the relativistic Bremsstrahlung cross section, Eq. (12); in particular, it involves the same screening functions  $I_{1,2}$ , defined by Eqs. (13) and (14), which we again evaluate using the Thomas-Fermi-Debye potential, Eq. (5), or its reduced form, as defined in Sec. II B 2. At high photon energies ( $\hbar\omega \gtrsim 100$  MeV), a Coulomb correction can also be applied to Eq. (25) (see formula 3D-1009 of Ref. 60 and the related discussion in Ref. 76) using the same additive factor  $-f_C$  as in the ultrarelativistic Bremsstrahlung cross section, Eq. (23).

Figure 8 illustrates the screening effects on the Bethe-Heitler cross section for a 10 and a 100 MeV photon incident on a solid-

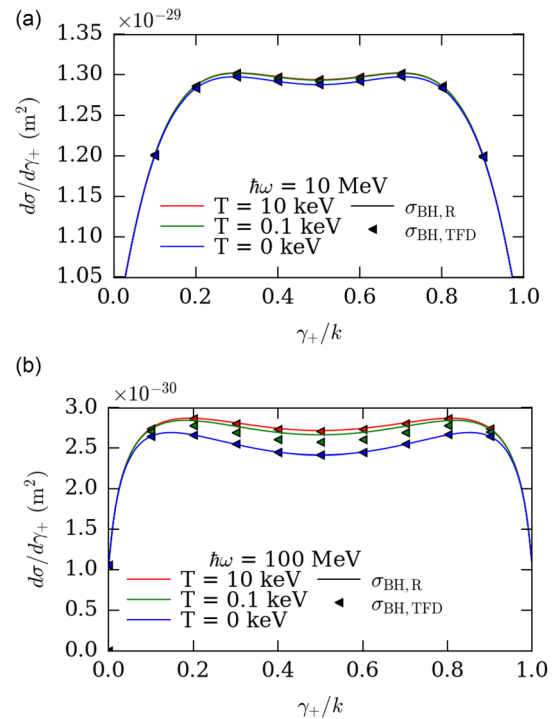


**FIG. 8.** Bethe-Heitler cross section vs normalized positron energy  $\gamma_+/k$  for a 10 MeV (a) and a 100 MeV (b) incident photon in a solid-density Cu plasma of temperature ranging from  $T = 0$  to 10 keV. The cross section computed numerically using the Thomas-Fermi-Debye potential ( $d\sigma_{BH,TFD}/d\gamma_+$ , symbols) closely matches the reduced analytical formula ( $d\sigma_{BH,R}/d\gamma_+$ , solid curves).  $k$  denotes the normalized photon energy  $k = \hbar\omega/mc^2$ .

density Cu plasma in the temperature range  $0 \leq T \leq 10$  keV. The cross section has a plateau-like shape symmetric with respect to  $\gamma_+ = k/2$ , of height (respectively, width) decreasing (respectively, increasing) with increased photon energy. For the 100 MeV photon energy considered here, the plateau extends from  $\gamma_+ \rightarrow 1$  to  $\gamma_+ \rightarrow k - 1$ . Similarly to the Bremsstrahlung, the cross section rises with the plasma temperature/ionization, and this behavior is more pronounced at large photon energies: The difference between the total cross section at  $T=0$  and 10 keV increases from  $\sim 0.5\%$  for  $\hbar\omega \leq 10$  MeV up to  $56\%$  for  $\hbar\omega = 10$  GeV. In the neutral case, we have checked that our formula satisfactorily matches the reference data of Hubbell *et al.*<sup>77</sup> For photon energies of 10 MeV and 100 MeV, the relative differences are measured to be of  $\sim 25\%$  and  $\sim 8\%$ , respectively.

#### D. Trident process

The Trident process corresponds to direct pair production by a high-energy electron in the Coulomb field of a nucleus. Due to the lack of tractable analytical formulas, screening effects on this process will be neglected here. Our approach reproduces that adopted by Vodopyanov *et al.*<sup>78</sup> Specifically, we use for the total Trident cross section the fitting formula provided by Gryaznykh,<sup>79</sup> based on the numerical evaluation of the cross section derived by Baier and Fadin,<sup>80</sup>

$$\sigma_T = 5.22Z^2 \ln^3 \left( \frac{\gamma_1 + 4.50}{6.89} \right) \times 10^{-34} \text{ m}^2, \quad (26)$$

where  $\gamma_1$  is the incident electron's Lorentz factor. It has recently been asserted<sup>81</sup> that this numerical fit may overestimate the exact cross section by a factor of  $\sim 4$ . Yet, in the absence of unambiguous theoretical proof, and in line with Refs. 78 and 82, we continue using it in its original form. The total (normalized) energy of the created pair ( $\gamma_p = \gamma_+ + \gamma_-$ ) is obtained from the singly differential cross sections calculated by Bhabha<sup>17</sup> in the low- and high-energy limits:

$$\frac{d\sigma_{T,nr}}{d\gamma_p} = \frac{(Zr_e\alpha_f)^2}{32} \times \left[ \log \gamma_1^2 - \frac{161}{60} + C + C_r + C_z \right] \times \frac{E_p^3}{(m_e c^2)^3}, \quad (p_+, p_-) \ll m_e c, \quad (27)$$

$$\frac{d\sigma_{T,r}}{d\gamma_p} = \frac{56}{9\pi} (Zr_e\alpha_f)^2 \ln \left( \frac{C_1 E_p}{m_e c^2} \right) \times \ln \left( \frac{C_2 m_e c^2 \gamma_1}{E_p} \right) \frac{m_e c^2}{E_p}, \quad (p_+, p_-) \gg m_e c, \quad (28)$$

where  $C_1$  and  $C_2$  are close to unity, and the coefficients  $C$ ,  $C_r$ , and  $C_z$  are given by

$$C_1 = C_2 = 1, \quad (29)$$

$$C = 4 \frac{x^2}{1-x^2} \log \frac{1}{x^2} - \frac{4}{3} x^2 + \frac{1}{6} x^4, \\ C_z = 3 \frac{x^2}{1-x^2} \left( 1 - \frac{x^2}{1-x^2} \log \frac{1}{x^2} \right) - \frac{13}{5} x^2 + \frac{7}{4} x^4 - \frac{9}{10} x^6 + \frac{1}{5} x^8, \\ C_r = -\frac{3}{2} \frac{x^2}{1-x^2} \left( 1 - \frac{x^2}{1-x^2} \log \frac{1}{x^2} \right) + \frac{4}{5} x^2 - \frac{1}{8} x^4 - \frac{1}{20} x^6 + \frac{1}{40} x^8,$$

where  $x = 1/\gamma_1$ .

An approximate cross section for arbitrary pair energies is obtained by the simple interpolation formula:

$$\frac{d\sigma_T}{d\gamma_p} = \frac{(d\sigma_{T,nr} d\gamma_p)(d\sigma_{T,r}/d\gamma_p)}{d\sigma_{T,nr}/d\gamma_p + d\sigma_{T,r}/d\gamma_p}. \quad (30)$$

Knowing the pair energy, the positron (or electron) energy is computed making use of the doubly differential cross section (32) of Ref. 17

$$\frac{d\sigma_T}{d\gamma_+} \propto \left( \gamma_+^2 + \gamma_-^2 + \frac{2}{3} \gamma_+ \gamma_- \right) \ln \frac{\gamma_+ \gamma_-}{\gamma_p}, \quad (31)$$

where  $\gamma_- = \gamma_p - \gamma_+$ . As in Ref. 78, we use this generic shape for the positron/electron distribution in the entire energy range even though, in principle, this formula holds only for  $\gamma_1 \gg (\gamma_+, \gamma_-) \gg 1$ .

### III. MONTE CARLO IMPLEMENTATION

#### A. Pairwise Bremsstrahlung algorithm with arbitrary macroparticle weights

We now describe the Monte Carlo implementation of the above photon and pair generation processes in the PIC code CALDER.<sup>44,83</sup> Binary interactions between macroparticles (or macrophotons) are treated using the pairwise collision scheme proposed by Nanbu and Yonemura,<sup>64</sup> as has been done previously for modeling impact ionization.<sup>65</sup> Since the same approach is applied to all processes, we focus on the Bremsstrahlung photon production in the following.

Let us define two populations of macroelectrons (index  $e$ ) and macroions (index  $i$ ). In a given mesh cell, the (physical) number density of species  $\alpha$  is given by  $n_\alpha = \sum_{k=1}^{N_\alpha} W_{\alpha k}$ , where  $W_{\alpha k}$  is the numerical weight of the  $k$ th macroparticle from species  $\alpha$ , and  $N_\alpha$  is the number of macroparticles of each species in the cell. Bremsstrahlung by electrons colliding with ions in a given cell is modeled by  $N_{ei} = \max(N_e, N_i)$  “macrointeractions” between electron-ion pairs, each pair being randomly sampled with a uniform probability.<sup>64</sup> The two macroparticles involved in the  $j$ th macrocollision ( $1 \leq j \leq N_{ei}$ ) are characterized by their Lorentz factor ( $\gamma_{\alpha j}$ ), momentum ( $\mathbf{p}_{\alpha j}$ ), velocity ( $\boldsymbol{\beta}_{\alpha j} = \mathbf{v}_{\alpha j}/c$ ), mass ( $m_{\alpha j}$ ), and the local density of their respective species.<sup>64,65</sup>

Since all the above cross sections are evaluated in the ion rest frame ( $K'$ ), it is convenient to express the electron momentum and energy from the simulation frame  $K$  to  $K'$  using the Lorentz transforms<sup>84</sup>

$$\mathbf{p}'_e = \mathbf{p}_e + \left[ \frac{\gamma_i - 1}{\beta_i^2} (\boldsymbol{\beta}_e \cdot \boldsymbol{\beta}_i) - \gamma_i \right] m_e c \gamma_e \boldsymbol{\beta}_e, \quad (32)$$

$$\gamma'_e = \gamma_e \gamma_i (1 - \boldsymbol{\beta}_e \cdot \boldsymbol{\beta}_i), \quad (33)$$

where the index  $j$  is omitted for simplicity. In the following, unprimed (respectively, primed) quantities are measured in frame  $K$  (respectively,  $K'$ ).

Given  $\sigma_B$  the total Bremsstrahlung cross section for an electron of energy  $\gamma_e$  and  $\mathbf{v}_{\text{rel}} = |\mathbf{v}_e - \mathbf{v}_i|$ , the probability of photon emission during a simulation time step  $\Delta t$  is

$$\mathcal{P}_B = 1 - \exp(-n_i \sigma_B \mathbf{v}_{\text{rel}} \Delta t). \quad (34)$$

Making use of the relativistic invariant  $\sigma_B \mathbf{v}_{\text{rel}} \gamma_e \gamma_i$ <sup>85</sup> and noting that  $\mathbf{v}'_{\text{rel}} = \mathbf{v}'_e$ , the above expression can be conveniently recast as



$$\mathcal{P}_B = 1 - \exp\left(-\frac{n_i \sigma'_B \gamma'_e v'_e}{\gamma_e \gamma_i} \Delta t\right). \quad (35)$$

Here,  $\sigma'_B$  denotes the Bremsstrahlung cross section in the ion rest frame, as evaluated in Sec. II B in various energy ranges.

Photon emission occurs if  $\mathcal{P}_B > U$ , where  $U \in [0; 1]$  is a uniform random number. A macrophoton is then created with an energy sampled from the numerical inversion of the cumulative distribution of  $d\sigma'_B/dk'$ . The resulting electron energy is  $\gamma'_{ef} = \gamma'_e - k'$ . Because  $d\sigma'_B/dk'$  diverges as  $1/k'$  when  $k' \rightarrow 0$ , the  $k'$ -interval is restricted to  $(10^{-n}, 1)$ , where  $n \in \mathbb{N}$ . The lower bound is chosen small enough that the radiated energy over the energy interval  $(0, 10^{-n})$  makes up a negligible fraction (typically  $\varepsilon = 10^{-5}$  for  $n=7$ ) of the total radiated energy. The photon is emitted at the electron location and parallel to the electron velocity. Finally, we compute the energy and momentum of the photon and decelerated electron in the simulation frame by means of an inverse Lorentz transformation.

The radiation probability (35) applies to an electron interacting with an ion population of density  $n_i$ . Yet in a PIC-Monte Carlo (PIC-MC) simulation, it has to be modified to take account of the random pairing process of macroparticles with different numerical weights. This is done following the method proposed in Refs. 64 and 65, whereby one macrocollision represents  $\min(W_{ej}, W_{ij})$  collisions between real particles. In the event of (physical) photon emission ( $\mathcal{P}_B > U$ ), the macrophoton is created (and the macroelectron is decelerated) with a probability  $P_{ej} = W_{ij}/\max(W_{ej}, W_{ij})$  and is then given the macroelectron's statistical weight  $W_{ej}$ . Introducing  $\Delta t_e$ , the interaction time step experienced by real electrons, its cell-averaged value is

$$\overline{\Delta t}_e = \Delta t_e \frac{\sum_{j=1}^{N_{ei}} W_{ej} P_{ej}}{n_e} \equiv \Delta t_e \frac{n_{ei}}{n_e}, \quad (36)$$

where we have defined  $n_{ei} = \sum_{j=1}^{N_{ei}} \min(W_{ej}, W_{ij})$ . Equating  $\overline{\Delta t}_e$  with the simulation time step  $\Delta t$  yields  $\Delta t_e = n_e \Delta t / n_{ei}$ . The Monte Carlo formulation of Eq. (35) is then

$$\mathcal{P}_B = 1 - \exp\left(-\frac{n_e n_i \sigma'_B \gamma'_e v'_e}{n_{ei} \gamma_e \gamma_i} \Delta t\right). \quad (37)$$

A similar scheme is used for the Bethe-Heitler and Trident processes. In the former case, the macrophotons and macroions are randomly paired in each cell, and the probability distribution is still of the form (37), with the difference that  $\sigma'_B$  is replaced by the (ion rest frame) total Bethe-Heitler cross section  $\sigma'_{BH}$ ,  $n_e$  by the photon density,  $n_i$ ,  $\gamma_e$  by  $k' \equiv \hbar\omega'/m_e c^2$ , and  $v'_e$  by  $c$ . In the event of pair production, the macrophoton is removed from the simulation, while the energies of the created electron and positron are sampled from the differential cross section  $d\sigma'_{BH}/d\gamma'_+$  given in Sec. II C 1. Both particles are emitted along the photon propagation direction.

Figures 9(a) and 9(b) illustrate the accuracy of our Monte Carlo Bremsstrahlung scheme in the case of a monoenergetic electron beam propagating through a neutral Cu medium. The beam electrons and background atoms are characterized by 1.6- $\mu\text{m}$ -long, uniform density profiles of densities  $n_e = 10^{21} \text{ cm}^{-3}$  and  $n_i = 8 \times 10^{22} \text{ cm}^{-3}$ , respectively. The beam electrons are initialized with an energy of 40 MeV, while the ions are taken to be at rest. The simulation, one-dimensional in

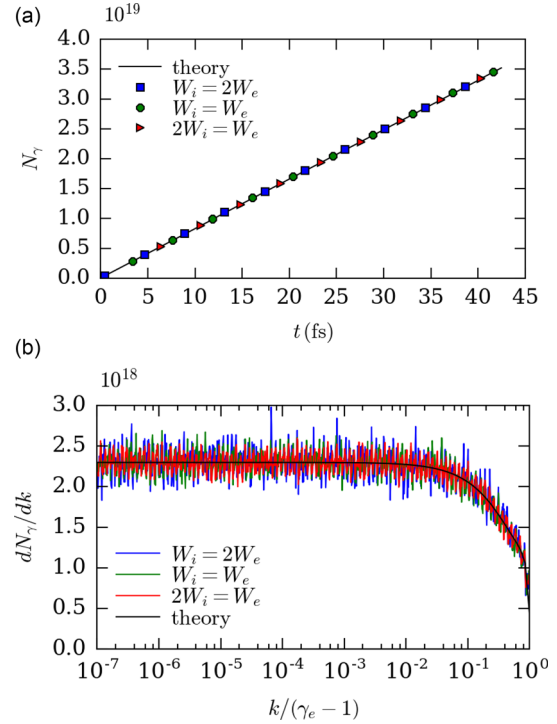


**FIG. 9.** (a) Total number and (b) energy spectrum (at  $t = 42$  fs) of the Bremsstrahlung photons generated by a 40 MeV electron beam (Lorentz factor  $\gamma_1$ ) incident on the neutral Cu atoms. Theoretical predictions [Eq. (38) in (a) and Eq. (39) in (b)] are represented with black lines. Three different weight ratios are employed:  $W_i/W_e = 2$  (blue), 1 (green), and 1/2 (red).

configuration space and the three-dimensional in velocity space (1D3V) employ periodic boundary conditions. Apart from Bremsstrahlung, all collective and collisional plasma processes are deactivated. The mesh size is  $\Delta x = 160$  nm, and the time step is  $\Delta t = 0.8\Delta x$ . Each cell contains 100 macroelectrons, while the number of macroions is varied, from 4000 to 16 000 per cell, such that the ion-to-electron weight ratio takes on three different values:  $W_i/W_e = 2, 1$  and  $1/2$ .

At early times (when variations in the electron beam energy are negligible), the total number of Bremsstrahlung photons and their energy spectra are expected to vary in time as

$$N_\gamma = n_e n_i v_e l \sigma_B t, \quad (38)$$

$$\frac{dN_\gamma}{dk} = n_e n_i v_e l \frac{d\sigma_B}{dk} t. \quad (39)$$

These evolution laws are well reproduced in Figs. 9(a) and 9(b) for the three values of  $W_i/W_e$  considered. This validates our Monte Carlo binary interaction scheme for modeling Bremsstrahlung. Similar validation tests have been performed for the Bethe-Heitler and Trident processes.

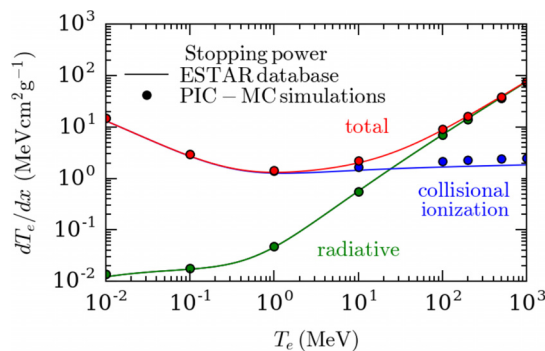
## B. Collisional-radiative stopping power in a neutral medium

The CALDER PIC-MC code now describes all the collisional and radiative processes accounting for the (noncollective) slowing down of

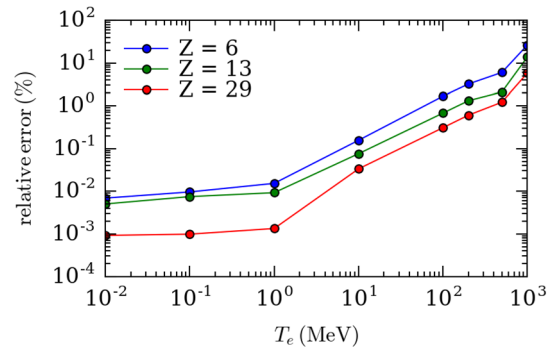
fast electrons through a dense assembly of ions or atoms. To illustrate this increased capability, we have performed a series of simulations of electron beam propagation through a neutral solid Cu target. These calculations are similar to those presented above except that both collisional ionization and Bremsstrahlung are now taken into account. The electron beam kinetic energy is varied in the range  $10^{-2} \leq T_1 \leq 10^3$  MeV. For each simulation, the stopping power is extracted by measuring the early-time energy loss rate of the test electrons, as resulting from collisional ionization,  $(dT/dx)_{\text{col}}$ , and Bremsstrahlung,  $(dT/dx)_{\text{rad}}$ . This measurement is made over the first time steps, during which the fraction of ionized atoms remains negligible. The collisional ionization scheme is detailed in Ref. 65, where a similar parametric scan is carried out in the nonradiative case.

Figure 10 plots the simulated values of  $(dT/dx)_{\text{col}}$  (blue markers),  $(dT/dx)_{\text{rad}}$  (green markers), and of the total stopping power  $(dT/dx)_{\text{tot}} = (dT/dx)_{\text{col}} + (dT/dx)_{\text{rad}}$  (red markers) as a function of  $T_1$ . Overall, the simulation results closely agree with the reference ESTAR (NIST) database<sup>86</sup> (solid lines). For  $T_1 \geq 10$  MeV, however, the PIC-MC simulation tends to overestimate the collisional (ionization) stopping power, due to the neglect of the density effect,<sup>87</sup> whose impact (in reducing the collisional stopping power) increases at large electron energies. This discrepancy does not affect much the accuracy of the PIC-MC modeled total stopping power because of the prevailing contribution of Bremsstrahlung at energies  $\geq 30$  MeV.

In the present pairwise algorithm, both Bremsstrahlung and collisional ionization are computed in the atom/ion rest frame, where their respective cross sections are known and tabulated. By contrast, elastic Coulomb collisions are usually treated in the center-of-mass frame, where they reduce to (identical) rotations of the interacting particles.<sup>52</sup> In Ref. 65, the latter frame was also employed for collisional ionization in order to speed up the calculation. This inconsistency can be tolerated insofar as the electron kinetic energy is small compared to the ion mass energy; in the opposite limit, it may lead to a significant error. This is shown in Fig. 11, which plots, for three types of neutral solid materials (C, Al, and Cu) and across a range of electron kinetic energies, the relative error in the collisional (ionization) stopping power made by working in the center-of-mass frame,  $(dT/dx)_{\text{col}}^{\text{com}}$ , instead of the atom rest frame,  $(dT/dx)_{\text{col}}^{\text{ion}}$ . For 1 GeV electrons, this error can reach  $\sim 20\%$  in carbon ( $Z=6$ ) and  $\sim 6\%$  in copper ( $Z=29$ ). At



**FIG. 10.** Collisional (blue), radiative (green), and total (red) stopping powers of the neutral solid copper ( $n_i = 6 \times 10^{22} \text{ cm}^{-3}$ ) as a function of the electron kinetic energy. Markers show the CALDER PIC-MC simulation results, while solid lines plot values from the ESTAR database.<sup>86</sup>



**FIG. 11.** Relative error in the PIC-MC collisional (ionization) stopping power resulting from working in the center-of-mass frame,  $(dT/dx)_{\text{col}}^{\text{com}}$ , rather than in the atom rest frame,  $(dT/dx)_{\text{col}}^{\text{ion}}$ , as a function of the electron kinetic energy, and for the three types of neutral solid materials.

electron energies  $\leq 100$  MeV, it remains  $\leq 2\%$  for the three atomic elements considered.

#### IV. PAIR GENERATION DURING RELAXATION OF FAST ELECTRONS IN A FINITE-SIZE PLASMA

We now illustrate the extended capability of the CALDER PIC code by investigating, in a self-consistent manner, the generation of electron-positron pairs by fast electrons in micrometer sized solid copper foils. This study is motivated by ongoing experimental research on pair generation by laser-driven relativistic electrons in solid targets.<sup>32–36,38</sup> Our main goal is to assess the impact of plasma effects on the competition between the indirect (Bethe-Heitler) and the direct (Trident) processes.

Our 1D3V (1D in configuration space and 3D in velocity space) simulation setup consists of a solid-density Cu plasma slab of thickness varying in the range  $5 \leq l \leq 15 \mu\text{m}$ . The Cu ions are initialized with a uniform density of  $8 \times 10^{22} \text{ cm}^{-3}$ , a temperature of 1 eV, and an ionization degree  $Z^* = 5$ . The fast electrons have a uniform density profile across the target and obey a 3D isotropic, relativistic Maxwell-Jüttner distribution,

$$f_e(T) = \frac{\gamma^2 \beta}{m_e c^2} \frac{\exp(-\gamma/\theta)}{\theta K_2(1/\theta)}, \quad (40)$$

where  $T = (\gamma - 1)m_e c^2$ ,  $\theta$  is the temperature normalized to  $m_e c^2$ , and  $K_2$  is a modified Bessel function of the second kind. In the following, use will be made of the average fast-electron kinetic energy  $\langle T \rangle / m_e c^2 = \int f_e(T) dT$ . For  $\theta \ll 1$ ,  $\langle T \rangle / m_e c^2 \simeq 3\theta/2$ , while for  $\theta \gg 1$ ,  $\langle T \rangle / m_e c^2 \simeq 3\theta$ . The simulation setup is depicted by the longitudinal  $x - p_x$  fast-electron phase space shown in Fig. 12. For  $l = 5, 10$ , and  $15 \mu\text{m}$ , the fast-electron density is set to  $n_e = 3 \times 10^{19} \text{ cm}^{-3}$ ,  $1.5 \times 10^{19} \text{ cm}^{-3}$ , and  $10^{19} \text{ cm}^{-3}$ , respectively, which corresponds to a constant areal density. Local charge neutrality is ensured by a bulk electron population of uniform density  $Z^* n_i - n_e$  and 1 eV temperature. To model the hydrogen-rich surface contaminants, the rear side of the Cu target is coated with a thin (6.25 nm) electron-proton layer of  $6 \times 10^{22} \text{ cm}^{-3}$  density (red curve). The plasma slab is centered around  $x = 80 \mu\text{m}$  in a  $286 \mu\text{m}$ -long simulation domain.

Our choice of a reduced 1D3V geometry is dictated by computational constraints: The spatiotemporal discretization should be fine

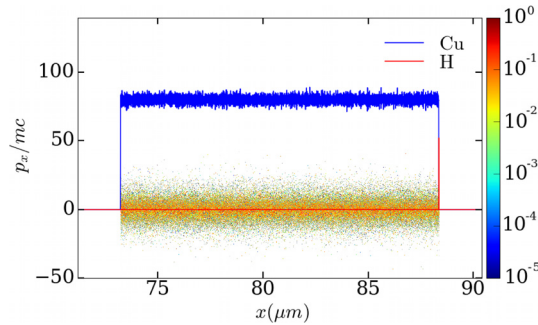


**FIG. 12.** 1D3V PIC simulation setup: Initial  $x - p_x$  phase space of the isotropic fast electron distribution (normalized to its maximum value) in a 15- $\mu\text{m}$ -thick copper target. The blue and red curves plot the density profiles of the bulk  $\text{Cu}^{5+}$  ions and rear-side contaminant protons.

enough to handle the large electron density (up to  $10^{24} \text{ cm}^{-3}$ ) of the highly ionized Cu plasma; the integration time should be long enough to reach the saturation of the pair generation. In order to quench numerical heating, the mesh size is set to  $\Delta x = 2.4 \text{ nm}$  (so that the simulation box comprises  $1.2 \times 10^5$  cells), and 4th order interpolation splines are employed. All simulations are run over  $2.5 \times 10^6$  iterations with time step  $\Delta t = 7.4 \times 10^{-3} \text{ fs}$ . Elastic collisions, the impact ionization, the Bremsstrahlung, the Bethe-Heitler, and the Coulomb Trident processes are all described. Note that the Bremsstrahlung, the Bethe-Heitler, and the Coulomb Trident processes are only simulated for the copper ions. The electron and carbon ion populations are initially represented by 50–150 macroparticles per cell depending on the target thickness. 1000 macroparticles per cell are used to model the thin hydrogen layer.

Figures 13(a) and 13(b) display the total number of positrons generated via the Bethe-Heitler (a) and Coulomb Trident (b) processes as a function of the initial average fast-electron kinetic energy ( $\langle T \rangle = 1 - 10 \text{ MeV}$ ) and the target thickness ( $l = 5 - 15 \mu\text{m}$ ). The positron yield is expressed per kilojoule of fast-electron kinetic energy. Also plotted are the predictions of the 0D theoretical model proposed by Myatt *et al.*<sup>82</sup> This model describes pair generation from both the Bethe-Heitler and Trident processes while taking into account collisional and radiative

decelerations of the fast electrons. The finite size of the target only intervenes in its optical depth for Bremsstrahlung photons. Perfect confinement of the fast electrons in the target is assumed. For the sake of consistency, we have included in this model the Bremsstrahlung and pair generation cross sections presented in Sec. II and considered a Maxwell-Jüttner energy distribution (40) for the fast electrons.

For both pair generation processes, the PIC simulations and the 0D model qualitatively agree in predicting an increasing trend in the positron yield with the fast-electron energy and the target thickness. Besides, they both indicate that the Trident process dominates pair generation at high electron energies and in thin targets. PIC simulations predict enhancements of the Bethe-Heitler and the Trident yields by factors of  $\sim 10$  and  $\sim 100$ , respectively, when  $\langle T \rangle$  rises from 1 MeV to 10 MeV. At  $\langle T \rangle = 5 \text{ MeV}$  (respectively, 10 MeV), the Trident process prevails in targets thicker than  $\sim 10 \mu\text{m}$  (respectively,  $15 \mu\text{m}$ ). While it gives the correct order of magnitude, the model tends to overestimate the positron yield, especially at large  $\langle T \rangle$  and small  $l$  for the Bethe-Heitler process. The discrepancy between the model and the PIC results is, however, more pronounced for the Trident process. Also, whereas the model predicts a Trident positron yield independent of the target thickness, the PIC values increase with  $l$ , although more slowly than for the Bethe-Heitler process.

The overestimation of the positron generation by the theoretical model stems from the neglect of energy losses associated with ion expansion. As is well-known,<sup>88,89</sup> the fast electrons set up an electrostatic field around the target boundaries. This sheath field, of strength  $E_x \propto \sqrt{n_e \langle T \rangle}$ , reflects the electrons back into the target while accelerating the surface ions outward. This ion expansion leads to cooling of the fast electrons.<sup>88,89</sup> This mechanism underlies the generation of energetic ion beams from laser-driven targets of a few micrometer thickness, in which context it is referred to as the target normal sheath acceleration (TNSA).<sup>90</sup> The energy transfer from the fast electrons to the ions is illustrated in Fig. 14, which plots the time evolution of the total (copper and hydrogen) ion kinetic energy normalized to the initial fast-electron energy,  $\langle T \rangle = 5 \text{ MeV}$ . As expected,<sup>89</sup> the energy conversion efficiency increases with thinner targets, from  $\sim 40\%$  at  $l = 15 \mu\text{m}$  to  $\sim 50\%$  at  $l = 5 \mu\text{m}$ . Note that such values likely overestimate owing to the absence of multidimensional effects (such as the transverse dilution of the fast electrons), which should cause the earlier saturation of the ion expansion.

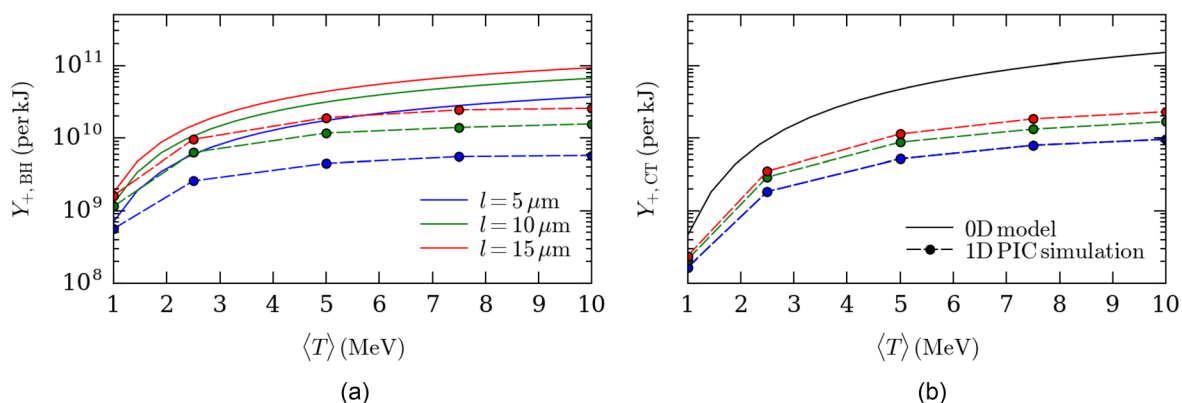


**FIG. 13.** (a) Bethe-Heitler and (b) Coulomb Trident positron yields vs average fast-electron kinetic energy for different thicknesses: Comparison of the 1D simulation results (dashed curves) and the predictions of Myatt's 0D theoretical model<sup>82</sup> (solid curves).

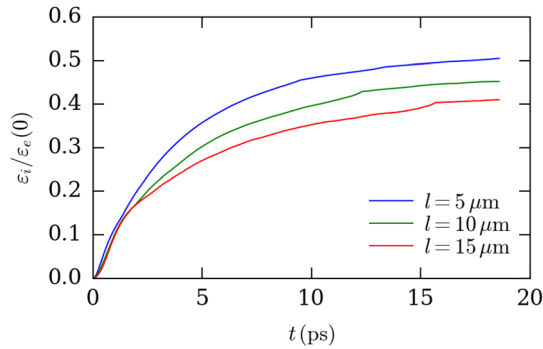


**FIG. 14.** Time evolution of the total ion kinetic energy normalized to the initial fast-electron kinetic energy for target thicknesses  $l \in (5, 10, 15) \mu\text{m}$ . The electrons are initially distributed according to a relativistic Maxwell-Jüttner law of average kinetic energy  $\langle T \rangle = 5 \text{ MeV}$ .

In the standard TNSA configuration (i.e., without positron generation), protons usually benefit the most from the fast-electron-induced sheath field due to their largest charge-to-mass ratio. Here, however, positrons are the lightest positively charged particles, and so respond the fastest to the sheath field while traveling across the target boundaries. The energy boost that they then undergo can strongly deform their energy spectrum, as evidenced experimentally.<sup>32</sup> The positron energy spectra plotted in Fig. 15 from both pair generation channels illustrate this mechanism in the case of  $\langle T \rangle = 10 \text{ MeV}$  and  $l = 15 \mu\text{m}$ : both spectra exhibit a bump accompanied by a plateau in the 5–20 MeV range, in contrast to the exponentially decreasing Bremsstrahlung photon spectrum.

To conclude this section, we note that, while manageable in the above-discussed simulations, the increasing number of macroparticles and macroparticles caused by photon and pair production processes may be a numerical issue in other configurations. To alleviate the computational load, one could resort to a combination of dynamic load balancing<sup>91</sup> and particle-merging schemes.<sup>92</sup>

## V. CONCLUSIONS

In summary, we have described a Monte Carlo numerical model for treating Bremsstrahlung, Bethe-Heitler, and Coulomb Trident

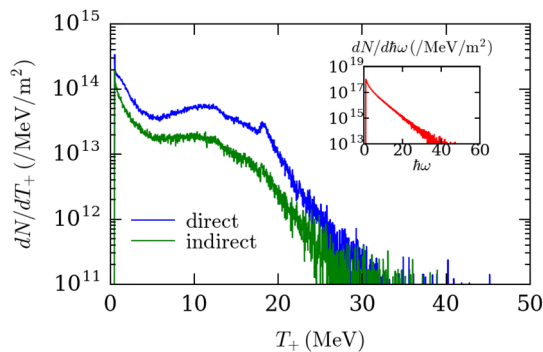


**FIG. 15.** Energy spectra of positrons generated via the Bethe-Heitler (green) and the Coulomb Trident (blue) processes for  $\langle T \rangle = 10 \text{ MeV}$  and  $l = 15 \mu\text{m}$ . The inset shows the corresponding photon energy spectrum.

processes in PIC simulations. For both Bremsstrahlung and Bethe-Heitler processes, we have first derived a set of analytical cross sections suited to arbitrary ionized media, making use of a Coulomb atomic potential that reproduces the Thomas-Fermi and Debye-type screened potentials expected, respectively, in the neutral and fully ionized limits. Overall, those formulas predict an increase in the cross sections at larger plasma temperatures due to a longer-range shielding. We have then developed a binary collision algorithm adapted to PIC simulations with weighted macroparticles/photons, which we have implemented into the PIC-MC CALDER code.<sup>7,65</sup> The accuracy of our numerical modeling has been benchmarked against the ESTAR electron stopping power database. Finally, we have examined the competition of the direct and indirect pair generation channels by a fast-electron population relaxing through a micrometric copper foil of varying thickness. While our 1D simulations qualitatively support the predictions of the 0D model of Myatt *et al.*,<sup>82</sup> the latter is shown to overestimate the yields of both pair generation processes due to the neglect of ion acceleration and of the corresponding electron energy loss. This collective plasma effect leads to an increasing discrepancy between the PIC and model results at larger fast-electron energies and thinner targets.

Thus upgraded, the PIC-MC CALDER code is now capable of capturing the full range of radiative (Bremsstrahlung, synchrotron) and pair generation (Bethe-Heitler, Coulomb Trident, Breit-Wheeler) mechanisms expected to arise in relativistic laser-plasma interactions, notably at the next-generation ELI-class laser facilities.<sup>11–14</sup> The numerical investigation of their interplay under various interaction conditions will be the subject of future work.

## ACKNOWLEDGMENTS

The authors acknowledge the helpful discussions with O. Embreus and T. Fülöp. PIC simulations were performed using HPC resources at TGCC/CCRT (GENCI Project No. A0010506129).

## APPENDIX A: NONRELATIVISTIC BREMSSTRAHLUNG CROSS SECTION WITH THOMAS-FERMI-DEBYE ATOMIC POTENTIAL

We detail here the derivation of the nonrelativistic, Bremsstrahlung differential cross section, Eq. (8). We start by calculating the Fourier transform (6) of the Thomas-Fermi-Debye potential (5), normalized by  $e/\alpha_f m_e c^2$ ,

$$\tilde{V}_{\text{TFD}}(u) = \frac{Z}{2\pi^2} \left\{ \frac{\eta_{\text{TF}} \tilde{L}_{\text{TF}}^2}{1 + \tilde{L}_{\text{TF}}^2 u^2} + \frac{\eta_{\text{D}} \tilde{L}_{\text{D}}^2}{1 + \tilde{L}_{\text{D}}^2 u^2} \right\}. \quad (\text{A1})$$

Substituting this expression into Eq. (7) yields

$$\begin{aligned} \frac{d\sigma_{\text{NR}}}{dk} = & \frac{64\pi^4 r_e^2 \alpha_f}{3kp_1^2} \left( \frac{Z}{2\pi^2} \right)^2 \times \left\{ \eta_{\text{TF}}^2 \tilde{L}_{\text{TF}}^4 \int_{\delta p_-}^{\delta p_+} \frac{u^3}{(1 + \tilde{L}_{\text{TF}}^2 u^2)^2} du \right. \\ & + \eta_{\text{D}}^2 \tilde{L}_{\text{D}}^4 \int_{\delta p_-}^{\delta p_+} \frac{u^3}{(1 + \tilde{L}_{\text{D}}^2 u^2)^2} du \\ & \left. + 2\eta_{\text{TF}} \eta_{\text{D}} \tilde{L}_{\text{TF}}^2 \tilde{L}_{\text{D}}^2 \int_{\delta p_-}^{\delta p_+} \frac{u^3}{(1 + \tilde{L}_{\text{TF}}^2 u^2)(1 + \tilde{L}_{\text{D}}^2 u^2)} du \right\}. \quad (\text{A2}) \end{aligned}$$



Each of these integrals can be analytically solved using standard methods, as detailed in Eqs. (D1) and (D6). The cross section then reads

$$\frac{d\sigma_{\text{NR}}}{dk} = \frac{16r_e^2\alpha_f Z^2}{3kp_1^2} \times \left\{ \frac{\eta_{\text{TF}}^2}{2} \left[ \ln \left( \frac{1 + \bar{L}_{\text{TF}}^2 \delta p_+^2}{1 + \bar{L}_{\text{TF}}^2 \delta p_-^2} \right) + \frac{1}{1 + \bar{L}_{\text{TF}}^2 \delta p_+^2} - \frac{1}{1 + \bar{L}_{\text{TF}}^2 \delta p_-^2} \right] + \frac{\eta_{\text{D}}^2}{2} \left[ \ln \left( \frac{1 + \bar{L}_{\text{D}}^2 \delta p_+^2}{1 + \bar{L}_{\text{D}}^2 \delta p_-^2} \right) + \frac{1}{1 + \bar{L}_{\text{D}}^2 \delta p_+^2} - \frac{1}{1 + \bar{L}_{\text{D}}^2 \delta p_-^2} \right] + \frac{\eta_{\text{TF}} \eta_{\text{D}}}{\bar{L}_{\text{TF}}^2 - \bar{L}_{\text{D}}^2} \left[ \bar{L}_{\text{TF}}^2 \ln \left( \frac{1 + \bar{L}_{\text{D}}^2 \delta p_+^2}{1 + \bar{L}_{\text{D}}^2 \delta p_-^2} \right) - \bar{L}_{\text{D}}^2 \ln \left( \frac{1 + \bar{L}_{\text{TF}}^2 \delta p_+^2}{1 + \bar{L}_{\text{TF}}^2 \delta p_-^2} \right) \right] \right\}, \quad (\text{A3})$$

which can be recast as Eq. (8).

## APPENDIX B: RELATIVISTIC BREMSSTRAHLUNG CROSS SECTION WITH A SINGLE-EXPONENTIAL ATOMIC POTENTIAL

We now consider the derivation of the relativistic Bremsstrahlung cross section, Eq. (12). Let us first introduce the electron ( $F_e$ ) and nucleus ( $F_n$ ) form factors,

$$F_{e,n}(\mathbf{u}) = \frac{1}{Z} \int d^3 \left( \frac{\mathbf{r}}{r_C} \right) \frac{r_C \rho_{e,i}(\mathbf{r})}{e} \exp \left( i \frac{\mathbf{u} \cdot \mathbf{r}}{r_C} \right), \quad (\text{B1})$$

where  $\rho_{e,n}(\mathbf{r})$  is the corresponding charge density. Assuming a point-like charge distribution for the nucleus,  $\rho_n = Ze\delta(\mathbf{r})$ , gives  $F_n = 1$ . From Poisson's equation, one can express the atomic form factor as a function of the Fourier transformed of the normalized potential

$$1 - F_e(u) = \frac{2\pi^2}{Z} u^2 \tilde{V}(u). \quad (\text{B2})$$

Since the atomic potential is taken to be spherically symmetric, the Fourier transformed potential (normalized by  $e/4\pi\epsilon_0$ ) can be simplified to

$$\tilde{V}(u) = \frac{1}{2\pi^2} \frac{e}{\alpha_f m_e c^2} \frac{1}{u} \int \frac{r}{r_C} V(r) \sin(ur/r_C) d\left(\frac{r}{r_C}\right). \quad (\text{B3})$$

In the case of a screened, single-exponential potential,  $V(r) = q \exp(-r/L)/r$  with  $q = Ze/4\pi\epsilon_0$ , one obtains

$$\tilde{V}(u) = \frac{Z}{2\pi^2} \frac{\bar{L}^2}{1 + \bar{L}^2 u^2}, \quad (\text{B4})$$

where we have used the relation  $r_e = \alpha_f r_C$ . We now evaluate the screening correction terms  $I_1$  and  $I_2$ . Using Eqs. (B2)–(B4) in Eq. (13) yields

$$I_1(\delta) = \bar{L}^4 \int_{\delta}^1 \frac{u^3}{(1 + \bar{L}^2 u^2)^2} du - 2\delta \bar{L}^4 \int_{\delta}^1 \frac{u^2}{(1 + \bar{L}^2 u^2)^2} du + \delta^2 \bar{L}^4 \int_{\delta}^1 \frac{u}{(1 + \bar{L}^2 u^2)^2} du. \quad (\text{B5})$$

These integrals have closed-form solutions; see Eqs. (D1)–(D3). There follows:

$$I_1(\delta) = \frac{1}{2} \left[ \ln \left( \frac{1 + \bar{L}^2}{1 + \bar{L}^2 \delta^2} \right) + \frac{1}{1 + \bar{L}^2} - \frac{1}{1 + \bar{L}^2 \delta^2} \right], \quad (\text{B6})$$

$$- \delta \left[ \bar{L} [\arctan(\bar{L}) - \arctan(\bar{L}\delta)] - \frac{\bar{L}^2}{1 + \bar{L}^2} + \frac{\delta \bar{L}^2}{1 + \bar{L}^2 \delta^2} \right], \quad (\text{B7})$$

$$+ \frac{\delta^2 \bar{L}^2}{2} \left[ \frac{1}{1 + \delta^2 \bar{L}^2} - \frac{1}{1 + \bar{L}^2} \right], \quad (\text{B8})$$

which can be readily simplified to Eq. (16).

We similarly proceed to calculate  $I_2$ . Combining Eq. (14) with Eqs. (B2)–(B4) gives

$$I_2(\delta) = \bar{L}^4 \int_{\delta}^1 \frac{u^3}{(1 + \bar{L}^2 u^2)^2} du - 6\delta^2 \bar{L}^4 \int_{\delta}^1 \frac{u \ln u}{(1 + \bar{L}^2 u^2)^2} du + 3\delta^2 \bar{L}^4 (2 \ln \delta + 1) \int_{\delta}^1 \frac{u}{(1 + \bar{L}^2 u^2)^2} du - 4\delta^3 \bar{L}^4 \int_{\delta}^1 \frac{1}{(1 + \bar{L}^2 u^2)^2} du. \quad (\text{B9})$$

Again, all of the above integrals can be analytically solved; see Eqs. (D1) and (D3)–(D5). One obtains  $I_2(\delta) = \sum_{i=1}^4 T_i(\delta)$  where

$$T_1(\delta) = \frac{1}{2} \left[ \ln \left( \frac{1 + \bar{L}^2}{1 + \bar{L}^2 \delta^2} \right) + \frac{1}{1 + \bar{L}^2} - \frac{1}{1 + \bar{L}^2 \delta^2} \right], \\ T_2(\delta) = 3\bar{L}^2 \delta^2 \left[ \frac{1}{2} \ln \left( \frac{1 + \bar{L}^2}{1 + \bar{L}^2 \delta^2} \right) + \frac{\bar{L}^2 \delta^2 \ln \delta}{1 + \bar{L}^2 \delta^2} \right], \\ T_3(\delta) = -\frac{3\delta^2 \bar{L}^2}{2} (1 + 2 \ln \delta) \left[ \frac{1}{1 + \bar{L}^2} - \frac{1}{1 + \bar{L}^2 \delta^2} \right], \\ T_4(\delta) = 2\delta^2 \bar{L}^2 \left[ \frac{\delta}{1 + \bar{L}^2} - \frac{1}{1 + \bar{L}^2 \delta^2} + 1 - \delta - \delta \bar{L} (\arctan(\bar{L}) - \arctan(\bar{L}\delta)) \right]. \quad (\text{B10})$$

Straightforward algebra then leads to the simplified expression Eq. (17).

## APPENDIX C: RELATIVISTIC BREMSSTRAHLUNG CROSS SECTION WITH THOMAS-FERMI-DEBYE ATOMIC POTENTIAL IN THE $\delta \rightarrow 0$ LIMIT

For the two-exponential Thomas-Fermi-Debye potential, Eq. (5), there is no general analytical expression for  $I_2(\delta)$ . However, in the limit  $\delta \rightarrow 0$ , both  $I_1$  and  $I_2$  converge to the same expression  $I_{\text{TFD}}$  defined by Eq. (18), which can be exactly calculated. Making use of Eqs. (A1) and (B2) leads to

$$I_{\text{TFD}} = \frac{q_{\text{TF}}^2 \bar{L}_{\text{TF}}^4}{q^2} \int_0^1 \frac{u^3}{(1 + \bar{L}_{\text{TF}}^2 u^2)^2} du + \frac{q_{\text{D}}^2 \bar{L}_{\text{D}}^4}{q^2} \int_0^1 \frac{u^3}{(1 + \bar{L}_{\text{D}}^2 u^2)^2} du + 2 \frac{q_{\text{TF}} q_{\text{D}}}{q^2} \bar{L}_{\text{TF}}^2 \bar{L}_{\text{D}}^2 \int_0^1 \frac{u^3}{(1 + \bar{L}_{\text{TF}}^2 u^2)(1 + \bar{L}_{\text{D}}^2 u^2)} du. \quad (\text{C1})$$

Substituting the closed-form expressions of the above integrals [see Eqs. (D1) and (D6)] directly yields Eq. (19).

## APPENDIX D: USEFUL INDEFINITE INTEGRALS

The following indefinite integrals are involved in the above calculations:

$$\int \frac{u^3}{(1 + \bar{L}^2 u^2)^2} du = \frac{1}{2\bar{L}^4} \left[ \ln(1 + \bar{L}^2 u^2) + \frac{1}{1 + \bar{L}^2 u^2} \right], \quad (D1)$$

$$\int \frac{u^2}{(1 + \bar{L}^2 u^2)^2} du = -\frac{1}{2\bar{L}^3} \left[ \frac{\bar{L}u}{1 + \bar{L}^2 u^2} - \arctan(\bar{L}u) \right], \quad (D2)$$

$$\int \frac{u}{(1 + \bar{L}^2 u^2)^2} du = -\frac{1}{2\bar{L}^2} \frac{1}{1 + \bar{L}^2 u^2}, \quad (D3)$$

$$\int \frac{1}{(1 + \bar{L}^2 u^2)^2} du = -\frac{1}{2\bar{L}^2} \left[ \frac{1}{u(1 + \bar{L}^2 u^2)} - \frac{1}{u} \bar{L} \arctan(\bar{L}u) \right], \quad (D4)$$

$$\int \frac{u \ln u}{(1 + \bar{L}^2 u^2)^2} du = -\frac{1}{2\bar{L}^2} \left[ \frac{\ln u}{1 + \bar{L}^2 u^2} - \ln u + \frac{1}{2} \ln(1 + \bar{L}^2 u^2) \right], \quad (D5)$$

$$\int \frac{u^3}{(1 + \bar{L}_\alpha^2 u^2)(1 + \bar{L}_\beta^2 u^2)} du = \frac{\bar{L}_\alpha^2 \ln(1 + \bar{L}_\beta^2 u^2) - \bar{L}_\beta^2 \ln(1 + \bar{L}_\alpha^2 u^2)}{2\bar{L}_\alpha^2 \bar{L}_\beta^2 (\bar{L}_\alpha^2 - \bar{L}_\beta^2)}. \quad (D6)$$

## REFERENCES

- <sup>1</sup>A. Di Piazza, C. Müller, K. Z. Hatsagortsyan, and C. H. Keitel, "Extremely high-intensity laser interactions with fundamental quantum systems," *Rev. Mod. Phys.* **84**, 1177–1228 (2012).
- <sup>2</sup>A. R. Bell and J. G. Kirk, "Possibility of prolific pair production with high-power lasers," *Phys. Rev. Lett.* **101**, 200403 (2008).
- <sup>3</sup>E. N. Nerush, I. Yu. Kostyukov, A. M. Fedotov, N. B. Narozhny, N. V. Elkina, and H. Ruhl, "Laser field absorption in self-generated electron-positron pair plasma," *Phys. Rev. Lett.* **106**, 035001 (2011).
- <sup>4</sup>C. P. Ridgers, C. S. Brady, R. Ducloux, J. G. Kirk, K. Bennett, T. D. Arber, A. P. L. Robinson, and A. R. Bell, "Dense electron-positron plasmas and ultraintense  $\gamma$  rays from laser-irradiated solids," *Phys. Rev. Lett.* **108**, 165006 (2012).
- <sup>5</sup>C. S. Brady, C. P. Ridgers, T. D. Arber, A. R. Bell, and J. G. Kirk, "Laser absorption in relativistically underdense plasmas by synchrotron radiation," *Phys. Rev. Lett.* **109**, 245006 (2012).
- <sup>6</sup>L. L. Ji, A. Pukhov, E. N. Nerush, I. Y. Kostyukov, B. F. Shen, and K. U. Akli, "Energy partition, gamma-ray emission, and radiation reaction in the near-quantum electrodynamic regime of laser-plasma interaction," *Phys. Plasmas* **21**(2), 023109 (2014).
- <sup>7</sup>M. Lobet, C. Ruyer, A. Debayle, E. d'Humières, M. Grech, M. Lemoine, and L. Gremillet, "Ultrafast synchrotron-enhanced thermalization of laser-driven colliding pair plasmas," *Phys. Rev. Lett.* **115**, 215003 (2015).
- <sup>8</sup>T. Grismayer, M. Vranic, J. L. Martins, R. A. Fonseca, and L. O. Silva, "Laser absorption via quantum electrodynamics cascades in counter propagating laser pulses," *Phys. Plasmas* **23**, 056706 (2016).
- <sup>9</sup>I. Y. Kostyukov and E. N. Nerush, "Production and dynamics of positrons in ultrahigh intensity laser-foil interactions," *Phys. Plasmas* **23**, 093119 (2016).
- <sup>10</sup>M. Lobet, X. Davoine, E. d'Humières, and L. Gremillet, "Generation of high-energy electron-positron pairs in the collision of a laser-accelerated electron beam with a multipetawatt laser," *Phys. Rev. Accel. Beams* **20**, 043401 (2017).
- <sup>11</sup>D. N. Papadopoulos, J. P. Zou, C. Le Blanc, L. Ranc, F. Druon, L. Martin, A. Fréneaux, A. Beluze, N. Lebas, M. Chabanis, C. Bonnin, J. B. Accary, B. L. Garrec, F. Mathieu, and P. Audebert, "First commissioning results of the apollo laser on the 1 pw beam line," in *Conference on Lasers and Electro-Optics* (Optical Society of America, 2019), p. STu3E.4.
- <sup>12</sup>J. H. Sung, H. W. Lee, J. Y. Yoo, J. W. Yoon, C. W. Lee, J. M. Yang, Y. J. Son, Y. H. Jang, S. K. Lee, and C. H. Nam, "4.2 PW, 20 fs Ti: Sapphire laser at 0.1 Hz," *Opt. Lett.* **42**(11), 2058–2061 (2017).
- <sup>13</sup>X. Zeng, K. Zhou, Y. Zuo, Q. Zhu, J. Su, X. Wang, X. Wang, X. Huang, X. Jiang, D. Jiang, Y. Guo, N. Xie, S. Zhou, Z. Wu, J. Mu, H. Peng, and F. Jing, "Multipetawatt laser facility fully based on optical parametric chirped-pulse amplification," *Opt. Lett.* **42**(10), 2014–2017 (2017).
- <sup>14</sup>S. Weber, S. Bechet, S. Borneis, L. Brabec, M. Bučka, E. Chacon-Golcher, M. Ciappina, M. DeMarco, A. Fajstavr, K. Falk, E.-R. Garcia, J. Grosz, Y.-J. Gu, J.-C. Hernandez, M. Holec, P. Janečka, M. Jantač, M. Jirka, H. Kadlecova, D. Khikhlikha, O. Klimo, G. Korn, D. Kramer, D. Kumar, T. Lastovička, P. Lutoslawski, L. Morejon, V. Olšovcová, M. Rajdl, O. Renner, B. Rus, S. Singh, M. Šmíd, M. Sokol, R. Versaci, R. Vrána, M. Vranic, J. Vyskočil, A. Wolf, and Q. Yu, "P3: An installation for high-energy density plasma physics and ultra-high intensity laser-matter interaction at eli-beamlines," *Matter Radiat. Extremes* **2**(4), 149–176 (2017).
- <sup>15</sup>H. W. Koch and J. W. Motz, "Bremsstrahlung cross-section formulas and related data," *Rev. Mod. Phys.* **31**, 920–955 (1959).
- <sup>16</sup>H. Bethe and W. Heitler, "On the stopping of fast particles and on the creation of positive electrons," *Proc. R. Soc. London A* **146**(856), 83–112 (1934).
- <sup>17</sup>H. J. Bhabha, "The creation of electron pairs by fast charged particles," *Proc. R. Soc. London A* **152**(877), 559–586 (1935).
- <sup>18</sup>J. D. Kmetec, C. L. Gordon, J. J. Macklin, B. E. Lemoff, G. S. Brown, and S. E. Harris, "MeV x-ray generation with a femtosecond laser," *Phys. Rev. Lett.* **68**, 1527–1530 (1992).
- <sup>19</sup>M. Schnürer, M. P. Kalashnikov, P. V. Nickles, Th. Schlegel, W. Sandner, N. Demchenko, R. Nolte, and P. Ambrosi, "Hard x-ray emission from intense short pulse laser plasmas," *Phys. Plasmas* **2**(8), 3106–3110 (1995).
- <sup>20</sup>M. D. Perry, J. A. Sefcik, T. Cowan, S. Hatchett, A. Hunt, M. Moran, D. Pennington, R. Snavely, and S. C. Wilks, "Hard x-ray production from high intensity laser solid interactions (invited)," *Rev. Sci. Instrum.* **70**(1), 265–269 (1999).
- <sup>21</sup>T. E. Cowan, A. W. Hunt, T. W. Phillips, S. C. Wilks, M. D. Perry, C. Brown, W. Fountain, S. Hatchett, J. Johnson, M. H. Key, T. Parnell, D. M. Pennington, R. A. Snavely, and Y. Takahashi, "Photonuclear fission from high energy electrons from ultraintense laser-solid interactions," *Phys. Rev. Lett.* **84**, 903–906 (2000).
- <sup>22</sup>M. I. K. Santala, M. Zepf, I. Watts, F. N. Beg, E. Clark, M. Tatarakis, K. Krushelnick, A. E. Dangor, T. McCanny, I. Spencer, R. P. Singhal, K. W. D. Ledingham, S. C. Wilks, A. C. Machacek, J. S. Wark, R. Allott, R. J. Clarke, and P. A. Norreys, "Effect of the plasma density scale length on the direction of fast electrons in relativistic laser-solid interactions," *Phys. Rev. Lett.* **84**, 1459–1462 (2000).
- <sup>23</sup>K. W. D. Ledingham, I. Spencer, T. McCanny, R. P. Singhal, M. I. K. Santala, E. Clark, I. Watts, F. N. Beg, M. Zepf, K. Krushelnick, M. Tatarakis, A. E. Dangor, P. A. Norreys, R. Allott, D. Neely, R. J. Clark, A. C. Machacek, J. S. Wark, A. J. Cresswell, D. C. W. Sanderson, and J. Magill, "Photonuclear physics when a multiterawatt laser pulse interacts with solid targets," *Phys. Rev. Lett.* **84**, 899–902 (2000).
- <sup>24</sup>Y. Glinec, J. Faure, L. Le Dain, S. Darbon, T. Hosokai, J. J. Santos, E. Lefebvre, J. P. Rousseau, F. Burgy, B. Mercier, and V. Malka, "High-resolution  $\gamma$ -ray radiography produced by a laser-plasma driven electron source," *Phys. Rev. Lett.* **94**, 025003 (2005).
- <sup>25</sup>J. Galy, M. Mau, D. J. Hamilton, R. Edwards, and J. Magill, "Bremsstrahlung production with high-intensity laser matter interactions and applications," *New. J. Phys.* **9**, 23 (2007).
- <sup>26</sup>C. D. Chen, P. K. Patel, D. S. Hey, A. J. Mackinnon, M. H. Key, K. U. Akli, T. Bartal, F. N. Beg, S. Chawla, H. Chen, R. R. Freeman, D. P. Higginson, A. Link, T. Y. Ma, A. G. MacPhee, R. B. Stephens, L. D. Van Woerkom, B. Westover, and M. Porkolab, "Bremsstrahlung and K $\alpha$  fluorescence measurements for inferring conversion efficiencies into fast ignition relevant hot electrons," *Phys. Plasmas* **16**(8), 082705 (2009).
- <sup>27</sup>B. Westover, A. MacPhee, C. Chen, D. Hey, T. Ma, B. Maddox, H.-S. Park, B. Remington, and F. N. Beg, "Study of silver K $\alpha$  and bremsstrahlung radiation from short-pulse laser-matter interactions with applications for x-ray radiography," *Phys. Plasmas* **17**(8), 082703 (2010).

- <sup>28</sup>A. Compant La Fontaine, C. Courtois, and E. Lefebvre, "Production of multi-MeV Bremsstrahlung x-ray sources by petawatt laser pulses on various targets," *Phys. Plasmas* **19**(2), 023104 (2012).
- <sup>29</sup>C. Courtois, R. Edwards, A. Compant La Fontaine, C. Aedy, S. Bazzoli, J. L. Bourgade, J. Gazave, J. M. Lagrange, O. Landoas, L. Le Dain, D. Mastrosimone, N. Pichoff, G. Pien, and C. Stoeckl, "Characterisation of a meV bremsstrahlung x-ray source produced from a high intensity laser for high areal density object radiography," *Phys. Plasmas* **20**(8), 083114 (2013).
- <sup>30</sup>T. E. Cowan, M. D. Perry, M. H. Key, T. R. Ditmire, S. P. Hatchett, E. A. Henry, J. D. Moody, M. J. Moran, D. M. Pennington, T. W. Phillips, T. C. Sangster, J. A. Sefcik, M. S. Singh, R. A. Snavely, M. A. Stoyer, S. C. Wilks, P. E. Young, Y. Takahashi, B. Dong, W. Fountain, T. Parnell, J. Johnson, A. W. Hunt, and T. Kuhl, "High energy electrons, nuclear phenomena and heating in petawatt laser-solid experiments," *Laser Part. Beams* **17**, 773–783 (1999).
- <sup>31</sup>C. Gahn, G. D. Tsakiris, G. Pretzler, K. J. Witte, C. Delfin, C.-G. Wahlström, and D. Habs, "Generating positrons with femtosecond-laser pulses," *Appl. Phys. Lett.* **77**, 2662 (2000).
- <sup>32</sup>H. Chen, S. C. Wilks, J. D. Bonlie, E. P. Liang, J. Myatt, D. F. Price, D. D. Meyerhofer, and P. Beiersdorfer, "Relativistic positron creation using ultraintense short pulse lasers," *Phys. Rev. Lett.* **102**, 105001 (2009).
- <sup>33</sup>H. Chen, S. C. Wilks, D. D. Meyerhofer, J. Bonlie, C. D. Chen, S. N. Chen, C. Courtois, L. Elbersson, G. Gregori, W. Kruer, O. Landoas, J. Mithen, J. Myatt, C. D. Murphy, P. Nilson, D. Price, M. Schneider, R. Shepherd, C. Stoeckl, M. Tabak, R. Tommasini, and P. Beiersdorfer, "Relativistic quasimonoenergetic positron jets from intense laser-solid interactions," *Phys. Rev. Lett.* **105**, 015003 (2010).
- <sup>34</sup>H. Chen, F. Fiuza, A. Link, A. Hazi, M. Hill, D. Hoarty, S. James, S. Kerr, D. D. Meyerhofer, J. Myatt, J. Park, Y. Sentoku, and G. J. Williams, "Scaling the yield of laser-driven electron-positron jets to laboratory astrophysical applications," *Phys. Rev. Lett.* **114**(21), 215001 (2015).
- <sup>35</sup>G. J. Williams, B. B. Pollock, F. Albert, J. Park, and H. Chen, "Positron generation using laser-wakefield electron sources," *Phys. Plasmas* **22**(9), 093115 (2015).
- <sup>36</sup>G. J. Williams, D. Barnak, G. Fiksel, A. Hazi, S. Kerr, C. Krauland, A. Link, M. J.-E. Manuel, S. R. Nagel, J. Park, J. Peebles, B. B. Pollock, F. N. Beg, R. Betti, and H. Chen, "Target material dependence of positron generation from high intensity laser-matter interactions," *Phys. Plasmas* **23**(12), 123109 (2016).
- <sup>37</sup>Y. Wu, K. Dong, Y. Yan, B. Zhu, T. Zhang, J. Chen, M. Yu, F. Tan, S. Wang, D. Han, F. Lu, and Y. Gu, "Pair production by high intensity picosecond laser interacting with thick solid target at XingGuangIII," *High Energy Density Phys.* **23**(Supplement C), 115–118 (2017).
- <sup>38</sup>G. Sarri, W. Schumaker, A. Di Piazza, M. Vargas, B. Dromey, M. E. Dieckmann, V. Chvykov, A. Maksimchuk, V. Yanovsky, Z. H. He, B. X. Hou, J. A. Nees, A. G. R. Thomas, C. H. Keitel, M. Zepf, and K. Krushelnick, "Table-top laser-based source of femtosecond, collimated, ultrarelativistic positron beams," *Phys. Rev. Lett.* **110**(25), 255002 (2013).
- <sup>39</sup>G. Sarri, K. Poder, J. Cole, W. Schumaker, A. Di Piazza, B. Reville, D. Doria, B. Dromey, L. Gizzi, A. Green, G. Grittani, S. Kar, C. H. Keitel, K. Krushelnick, S. Kushel, S. Mangles, Z. Najmudin, A. G. R. Thomas, M. Vargas, and M. Zepf, "Generation of a neutral, high-density electron-positron plasma in the laboratory," *Nat. Commun.* **6**, 6747 (2015).
- <sup>40</sup>T. Xu, B. Shen, J. Xu, S. Li, Y. Yu, J. Li, X. Lu, C. Wang, X. Wang, X. Liang, Y. Leng, R. Li, and Z. Xu, "Ultrashort megaelectronvolt positron beam generation based on laser-accelerated electrons," *Phys. Plasmas* **23**(3), 033109 (2016).
- <sup>41</sup>E. Liang, T. Clarke, A. Henderson, W. Fu, W. Lo, D. Taylor, P. Chaguine, S. Zhou, Y. Hua, X. Cen, X. Wang, J. Kao, H. Hasson, G. Dyer, K. Serrat, N. Riley, M. Donovan, and T. Ditmire, "High e<sup>+</sup>/e<sup>-</sup> Ratio Dense Pair Creation with 10<sup>21</sup> W cm<sup>-2</sup> Laser Irradiating Solid Targets," *Sci. Rep.* **5**, 13968 (2015).
- <sup>42</sup>C. K. Birdsall and A. B. Langdon, *Plasma Physics via Computer Simulation*. Series in Plasma Physics (Taylor & Francis, New York, 2004).
- <sup>43</sup>R. Duclos, J. G. Kirk, and A. R. Bell, "Monte Carlo calculations of pair production in high-intensity laser-plasma interactions," *Plasma Phys. Controlled Fusion* **53**(1), 015009 (2011).
- <sup>44</sup>M. Lobet, E. d'Humières, M. Grech, C. Ruyer, X. Davoine, and L. Gremillet, "Modeling of radiative and quantum electrodynamics effects in pic simulations of ultra-relativistic laser-plasma interaction," *J. Phys. Conf. Ser.* **688**(1), 012058 (2016).
- <sup>45</sup>L. Yi, A. Pukhov, P. Luu-Thanh, and B. Shen, "Bright X-ray source from a laser-driven microplasma waveguide," *Phys. Rev. Lett.* **116**, 115001 (2016).
- <sup>46</sup>R. R. Pandit and Y. Sentoku, "Higher order terms of radiative damping in extreme intense laser-matter interaction," *Phys. Plasmas* **19**(7), 073304 (2012).
- <sup>47</sup>A. Gonoskov, S. Bastrakov, E. Efimenko, A. Ilderton, M. Marklund, I. Meyerov, A. Muraviev, A. Sergeev, I. Surmin, and E. Wallin, "Extended particle-in-cell schemes for physics in ultrastrong laser fields: Review and developments," *Phys. Rev. E* **92**, 023305 (2015).
- <sup>48</sup>A. Henderson, E. Liang, P. Yepes, H. Chen, and S. C. Wilks, "Monte Carlo simulation of pair creation using petawatt lasers," *Astrophys. Space Sci.* **336**, 273 (2011).
- <sup>49</sup>Y. Yan, Y. Wu, Z. Zhao, J. Teng, J. Yu, D. Liu, K. Dong, L. Wei, W. Fan, L. Cao, Z. Yao, and Y. Gu, "Monte Carlo simulation study of positron generation in ultra-intense laser-solid interactions," *Phys. Plasmas* **19**(2), 023114 (2012).
- <sup>50</sup>Y. Yan, K. Dong, Y. Wu, B. Zhang, Z. Yao, and Y. Gu, "Numerical simulation study of positron production by intense laser-accelerated electrons," *Phys. Plasmas* **20**(10), 103106 (2013).
- <sup>51</sup>S. Jiang, A. G. Krygier, D. W. Schumacher, K. U. Akli, and R. D. Freeman, "Enhancing Bremsstrahlung production from ultraintense laser-solid interactions with front surface structures," *Eur. Phys. J. D* **68**, 283 (2014).
- <sup>52</sup>Y. Sentoku, K. Mima, T. Taguchi, S. Miyamoto, and Y. Kishimoto, "Particle simulation on x-ray emissions from ultra-intense laser produced plasmas," *Phys. Plasmas* **5**(12), 4366–4372 (1998).
- <sup>53</sup>S. N. Andreev, S. G. Garanin, A. A. Rukhadze, V. P. Tarakanov, and B. P. Yakutov, "Simulation of generation of bremsstrahlung gamma quanta upon irradiation of thin metal films by ultra-intense femtosecond laser pulses," *Quantum Electron.* **40**, 355–362 (2010).
- <sup>54</sup>R. Ward and N. J. Sircombe, "Fast particle Bremsstrahlung effects in the PIC code EPOCH: Enhanced diagnostics for laser-solid interaction modeling," Central Laser Facility Annual Report 2013–2014, 2014.
- <sup>55</sup>J. Vyskočil, O. Klimo, and S. Weber, "Simulations of bremsstrahlung emission in ultra-intense laser interactions with foil targets," *Plasma Phys. Controlled Fusion* **60**(5), 054013 (2018).
- <sup>56</sup>D. Wu, X. T. He, W. Yu, and S. Fritzsche, "Particle-in-cell simulations of laser-plasma interactions at solid densities and relativistic intensities: The role of atomic processes," *High Power Laser Sci. Eng.* **6**, e50 (2018).
- <sup>57</sup>T. Moritaka, L. Baiotti, A. Lin, L. Weiwi, Y. Sakawa, Y. Kuramitsu, T. Morita, and H. Takabe, "Plasma particle-in-cell simulations with qed reactions for pair production experiments using a high-z solid target," *J. Phys.: Conf. Ser.* **454**(1), 012016 (2013).
- <sup>58</sup>T. Nakamura and T. Hayakawa, "Numerical modeling of quantum beam generation from ultra-intense laser-matter interactions," *Laser Part. Beams* **33**(2), 151–155 (2015).
- <sup>59</sup>S. M. Seltzer and M. J. Berger, "Bremsstrahlung energy spectra from electrons with kinetic energy 1 keV–10 GeV incident on screened nuclei and orbital electrons of neutral atoms with Z = 1,100," *At. Data Nucl. Data Tables* **35**(3), 345–418 (1986).
- <sup>60</sup>J. W. Motz, H. A. Olsen, and H. W. Koch, "Pair Production by Photons," *Rev. Mod. Phys.* **41**, 581–639 (1969).
- <sup>61</sup>E. Nardi and Z. Zinamon, "Energy deposition by relativistic electrons in high-temperature targets," *Phys. Rev. A* **18**, 1246–1249 (1978).
- <sup>62</sup>E. Nardi, E. Y. Maron, and D. H. H. Hoffmann, "Plasma diagnostics by means of the scattering of electrons and proton beams," *Laser Part. Beams* **25**, 489–495 (2007).
- <sup>63</sup>B. F. Rozsnyai, "Computation of free-free Gaunt factors and conductive opacities in hot matter," *J. Quant. Spectrosc. Radiat. Transfer* **22**, 337–343 (1979).
- <sup>64</sup>K. Nanbu and S. Yonemura, "Weighted particles in Coulomb collision simulations based on the theory of a cumulative scattering angle," *J. Comput. Phys.* **145**(2), 639–654 (1998).
- <sup>65</sup>F. Pérez, L. Gremillet, A. Decoster, M. Drouin, and E. Lefebvre, "Improved modeling of relativistic collisions and collisional ionization in particle-in-cell codes," *Phys. Plasmas* **19**(8), 083104 (2012).
- <sup>66</sup>G. Molière, "Theorie der Streuung schneller geladener Teilchen I. Einzelstreuung am abgeschirmten Coulomb-Feld," *Z. Naturforsch. A* **2**, 133–145 (1947).
- <sup>67</sup>N. H. March, "The Thomas-Fermi approximation in quantum mechanics," *Adv. Phys.* **6**, 1 (1957).

- <sup>68</sup>Y. T. Lee and R. M. More, "An electron conductivity model for dense plasmas," *Phys. Fluids* **27**, 1273–1286 (1984).
- <sup>69</sup>R. M. More, "Pressure ionization, resonances, and the continuity of bound and free states," *Adv. At. Mol. Phys.* **21**, 305–356 (1985).
- <sup>70</sup>M. Das, B. K. Sahoo, and S. Pal, "Plasma screening effects on the electronic structure of multiply charged Al ions using Debye and ion-sphere models," *Phys. Rev. A* **93**(5), 052513 (2016).
- <sup>71</sup>W. Heitler, *The Quantum Theory of Radiation*. Monographs on Physics (Oxford University Press, 1954).
- <sup>72</sup>G. Elwert, "Verschärfte Berechnung von Intensität und Polarisation im kontinuierlichen Röntgenspektrum," *Ann. Phys.* **426**, 178–208 (1939).
- <sup>73</sup>S. M. Seltzer and M. J. Berger, "Bremsstrahlung spectra from electron interactions with screened atomic nuclei and orbital electrons," *Nucl. Instrum. Methods Phys. Res. B* **12**(1), 95–134 (1985).
- <sup>74</sup>H. A. Bethe and N. F. Mott, "The influence of screening on the creation and stopping of electrons," *Proc. Cambridge Philos. Soc.* **30**, 524 (1934).
- <sup>75</sup>Y. S. Tsai, "Pair production and bremsstrahlung of charged leptons," *Rev. Mod. Phys.* **46**, 815–851 (1974).
- <sup>76</sup>F. Salvat and J. M. Fernández-Varea, "Overview of physical interaction models for photon and electron transport used in Monte Carlo codes," *Metrologia* **46**(2), S112–S138 (2009).
- <sup>77</sup>J. H. Hubbell, H. A. Gimm, and I. Overbo, "Pair, triplet, and total atomic cross sections (and mass attenuation coefficients) for 1 mev 100 gev photons in elements  $z=1$  to 100," *J. Phys. Chem. Ref. Data* **9**(4), 1023–1148 (1980).
- <sup>78</sup>I. B. Vodopyanov, J. R. Dwyer, E. S. Cramer, R. J. Lucia, and H. K. Rassoul, "The effect of direct electron-positron pair production on relativistic feedback rates," *J. Geophys. Res.* **120**, 800–806, <https://doi.org/10.1002/2014JA020415> (2015).
- <sup>79</sup>D. A. Gryaznykh, Y. Z. Kandiev, and V. A. Lykov, "Estimates of electron-positron pair production in the interaction of high-power laser radiation with high-Z targets," *JETP Lett.* **67**(4), 257–262 (1998).
- <sup>80</sup>V. N. Baier and V. S. Fadin, "Electroproduction of pairs of particles at high energies," *Sov. Phys. JETP* **34**, 253 (1972).
- <sup>81</sup>O. Embréus, L. Hesslow, M. Hoppe, G. Papp, K. Richards, and T. Fülöp, "Dynamics of positrons during relativistic electron runaway," *J. Plasma Phys.* **84**(5), 905840506 (2018).
- <sup>82</sup>J. Myatt, J. A. Delettrez, A. V. Maximov, D. D. Meyerhofer, R. W. Short, C. Stoeckl, and M. Storm, "Optimizing electron-positron pair production on kilojoule-class high-intensity lasers for the purpose of pair-plasma creation," *Phys. Rev. E* **79**, 066409 (2009).
- <sup>83</sup>E. Lefebvre, N. Cochet, S. Fritzler, V. Malka, M.-M. Aléonard, J.-F. Chemin, S. Darbon, L. Disdier, J. Faure, A. Fedotoff, O. Landoas, G. Malka, V. Méot, P. Morel, M. R. LeGloahec, A. Rouyer, C. Rubbelynck, V. Tikhonchuk, R. Wrobel, P. Audebert, and C. Rousseaux, "Electron and photon production from relativistic laser plasma interactions," *Nucl. Fusion* **43**, 629–633 (2003).
- <sup>84</sup>J. D. Jackson, *Classical Electrodynamics* (John Wiley, New York, 1975).
- <sup>85</sup>L. D. Landau and E. M. Lifshitz, *The Classical Theory of Fields* (Pergamon Press, Oxford, 1975).
- <sup>86</sup>M. J. Berger, J. S. Coursey, M. A. Zucker, and J. Chang, Estar, pstar, and astar: Computer programs for calculating stopping-power and range tables for electrons, protons, and helium ions (version 2.0.0), 2017.
- <sup>87</sup>R. M. Sternheimer, "Density effect for the ionization loss of charged particles," *Phys. Rev.* **145**, 247–250 (1966).
- <sup>88</sup>P. Mora, "Plasma expansion into a vacuum," *Phys. Rev. Lett.* **90**, 185002 (2003).
- <sup>89</sup>P. Mora, "Thin-foil expansion into a vacuum," *Phys. Rev. E* **72**, 056401 (2005).
- <sup>90</sup>A. Macchi, M. Borghesi, and M. Passoni, "Ion acceleration by superintense laser-plasma interaction," *Rev. Mod. Phys.* **85**, 751–793 (2013).
- <sup>91</sup>K. Geraschewski, W. Fox, S. Abbott, N. Ahmadi, K. Maynard, L. Wang, H. Ruhl, and A. Bhattacharjee, "The plasma simulation code: A modern particle-in-cell code with patch-based load-balancing," *J. Comput. Phys.* **318**, 305–326 (2016).
- <sup>92</sup>M. Vranic, T. Grismayer, J. L. Martins, R. A. Fonseca, and L. O. Silva, "Particle merging algorithm for {PIC} codes," *Comput. Phys. Commun.* **191**, 65–73 (2015).